Geometric and temporal evolution of extensional growth folds in the Barents Sea, offshore Norway: A tool to understand normal fault growth

Ahmed Alghuraybi[1]*, Rebecca E. Bell[1], Christopher A-L. Jackson[2]

[1]*Basins Research Group (BRG), Earth Science and Engineering, Imperial College, Prince Consort Road, London, SW7 2BP, UK*

[2]*Department of Earth, Atmospheric and Environmental Sciences, The University of Manchester, Williamson Building, Oxford Road, Manchester, M13 9PL, UK*

**Corresponding author: Ahmed Alghuraybi (a.alghuraybi19@imperial.ac.uk)*

Abstract

Extensional growth folds form ahead of the tips of propagating normal faults. These folds can accommodate a considerable amount of extensional strain and they may control rift geometry. Fold-related surface deformation may also control the sedimentary evolution of syn-rift depositional systems; thus, the stratigraphic record can constrain the four-dimensional evolution of extensional growth folds, which in term provides a record of fault growth and broader rift history. Here we use high-quality 3D seismic reflection and borehole data from the SW Barents Sea, offshore northern Norway to determine the geometric and temporal evolution of extensional growth folds associated with a large, long-lived, basement-involved fault. We show that the fault grew via linkage of four segments, and that fault growth was associated with the formation of fault-parallel and fault-perpendicular folds that accommodated a substantial portion (10 – 40%) of the total extensional strain. Fault-propagation folds formed at multiple times in response to periodic burial of the causal fault, with individual folding events (c. 25 Myr and 32 Myr) lasting a considered part of the total, c. 130 Myr rift period. Our study supports previous suggestions that continuous (i.e., folding) as well as discontinuous (i.e., faulting) deformation must be explicitly considered when assessing total strain in extensional setting. We also show changes in the architecture of growth strata record alternating periods of how folding and faulting, showing how rift margins may be characterised by basinward-dipping monoclines as opposed to fault-bound scarps. Our findings have broader implications for our understanding of the structural, physiographic, and tectonostratigraphic evolution of rift basins.

Key words: Normal Fault Growth, Extensional Growth Folds, Continuous Strain, Strike-Projections , Barents Sea

Introduction

Basin-bounding normal fault systems have a complex three-dimensional geometry, typically consisting of variably linked segments that branch along both the strike and dip directions (e.g. Walsh et al., 1999, 2002, 2003; Childs et al., 2002; van der Zee & Urai, 2005; Schöpfer et al., 2006; Long & Imber, 2010; Giba et al., 2012; Jackson & Rotevatn, 2013; Fossen & Rotevatn, 2016; Freitag et al., 2017; Camanni et al., 2019; Deng & McClay, 2021). These geometries reflect the fact that basin-bounding normal fault systems evolve via the growth, interaction, and linkage of smaller segments (e.g. Jackson, 1987; Schlische, 1992; Morley, 1999; Gawthorpe & Leeder, 2000; McLeod et al., 2000; Peacock, 2002). How faults grow has significant implications for the structural, physiographic, and tectonostratigraphic evolution of rift basins, as well as their potential for hosting energy resources and for sequestering CO2 (Gawthorpe & Leeder, 2000; Childs et al., 2017; Jackson et al., 2017; Michie et al., 2021).

Fault growth patterns also control the development of growth folds (also known as fault-propagation folds); these structures form ahead of the propagating normal fault tips and typically form during the early phases of extension, accommodating a considerable amount of extensional strain (e.g. Withjack et al., 1990; Allmendinger, 1998; Cosgrove & Ameen, 1999; Hardy & McClay, 1999; Gawthorpe & Leeder, 2000; Withjack & Callaway, 2000; Coleman et al., 2019; Jackson et al., 2020). Growth folds play a major role in controlling rift geometry and the sedimentary evolution of syn-rift systems as they alter sediment-transport pathways, and act as sediment sources if eroded (e.g. Laubscher, 1982; Maurin & Niviere, 1999; Gawthorpe & Leeder, 2000; Sharp et al., 2000; Lewis et al., 2015; Jackson & Lewis, 2016; Coleman et al., 2019). Geometrically complex hanging wall fold and fault geometries can develop within a single regional extensional stress regime without invoking any changes in the regional stresses (e.g. Khalil & McClay, 2018), although multiphase extension, fault segmentation, and changes in regional stress regime can result in additional, four-dimensionally complexity (Conneally et al., 2017; Deng & McClay, 2019; Jackson et al., 2020). For example, along strike variations in displacement along segmented normal faults mean breached and un-breached growth folds are spatially and temporally related (e.g. Gawthorpe et al., 1997; Gupta et al., 1999; Corfield & Sharp, 2000; Sharp et al., 2000; Corfield et al., 2001; Khalil & McClay, 2002; Willsey et al., 2002; White & Crider, 2006; Lewis et al., 2013; Lewis et al., 2015; Khalil & McClay, 2017; Coleman et al., 2019; Jackson et al., 2020). These structural dynamics are often recorded in the stratigraphic architecture of and facies distributions within hanging wall depocenters formed next to fault-fold systems (Gawthorpe et al., 1997; Corfield & Sharp, 2000; Sharp et al., 2000; Kane et al., 2010; Duffy et al., 2013; Coleman et al., 2019). Extensional growth folds also vary in shape and size across the fault surface as a function of, for example, the depth at which faults nucleate, changes in host rock lithology and rheology, and dip linkage between initially isolated segments (e.g. Mansfield & Cartwright, 2000; Rykkelid & Fossen, 2002). Despite containing a record of fault growth and broader rift history, few studies have attempted to analyse extensional growth folds in four dimensions using borehole and 3D seismic reflection data (e.g. Gawthorpe et al., 1997; Corfield et al., 2001; Patton, 2004; Lewis et al., 2015; Coleman et al., 2019; McHarg et al., 2020; Long & Imber, 2010; Conneally et al., 2017; Deng & McClay, 2019). Such data are optimal for this purpose, given they reveal the present basin structure and stratigraphic architecture, and allow inferences to be made regarding the underlying kinematics

In this study, we use high-quality 3D seismic reflection and borehole data from the SW Barents Sea, offshore northern Norway to provide a detailed analysis of the geometric and temporal evolution of extensional growth folding associated with part of a large, basement-involved fault (c. 30 km long, c. 2 km maximum displacement). This fault forms part of the Troms-Finnmark Fault Complex (TFFC), a basement-involved, rift-related structure that accommodated several phases of Palaeozoic to Cenozoic extension. Combining both 3D seismic reflection and borehole data enables us to study the temporal evolution of this fault system using age-constrained synkinematic stratigraphy. By doing this we show how large, crustal-scale faults and their associated folds evolve and control rift structure and sedimentation over timescales of c. 100 Myr.

Geological Setting

Regional Tectonics

The Barents Sea is a shallow continental shelf located in the northwest corner of the Eurasian tectonic plate, between the Arctic Ocean to the north, and the Russian and Norwegian coastlines to the south (Gabrielsen, 1984) (Fig. 1). The SW Barents Sea is presently a passive margin that consists of numerous predominately NNE-trending rift basins and basement highs (Faleide et al., 1984, 1993, 2008). Multiple phases of rifting occurred in the Barents Sea, initiated by the Devonian collapse of the Caledonian Orogeny, and concluding with the opening of the Norwegian and Greenland Seas and the onset of seafloor spreading in the Eocene (Faleide et al., 1984, 1993, 2008; Gabrielsen, 1984; Gabrielsen et al., 2016). The late Cambrian to mid-Devonian Caledonian Orogeny formed the crystalline basement rocks of the SW Barents Sea (Faleide et al., 1984). The large-scale fabric of these Caledonian igneous and metamorphic rocks played a major role in shaping the evolution and present structural framework of the area (see below; e.g., Faleide et al., 1984; Ritzmann & Faleide, 2007).

At least four distinct rift phases controlled the long-term evolution and large-scale structure of the SW Barents Sea based on seismic reflection, wide-angle refraction and potential field data; ?Late Devonian – Carboniferous, Late Permian, Middle Jurassic – Early Cretaceous, and Paleocene – Eocene (Faleide et al., 2008). Crustal extension in the ?Late Devonian – Carboniferous created N- to NE-trending half-grabens and resulted in the formation of the TFFC (e.g. Gabrielsen, 1984; Faleide et al., 2008; Indrevær et al., 2013). The TFFC is a basement-involved normal fault system that represents a major structural element of the SW Barents Sea, separating recent shelf sediments from onshore crystalline basement rocks (e.g. Gabrielsen, 1984; Indrevær et al., 2013). The TFFC runs parallel to the present-day coastline of Norway, striking NE-SW in its southernmost part and NW-SE in its northern part (Gabrielsen, 1984). Previous studies of the TFFC based on seismic reflection and potential field data suggest that it was continually reactivated until the Eocene (Gabrielsen et al., 1984; Faleide et al., 1993).

In the latest Carboniferous to Permian and following the first phase of rifting, the newly formed narrow basins were filled with evaporites and carbonates, which were later covered by clastic rocks (Faleide et al., 1984). Clastic sedimentation continued during the second phase of rifting in the Late Permian, which created considerable accommodation (e.g. Johansen et al., 1993; Larssen et al., 2002). The Triassic was a period of moderate tectonic activity that saw high subsidence and clastic sediment accumulation rates, and which ended with a regional marine transgression (e.g. Glørstad-Clark et al., 2010; Harishidayat et al., 2015; Mattos et al., 2016).

During the Middle Jurassic – Early Cretaceous, a third, intense phase of rifting occurred in the SW Barents Sea, resulting in the formation of multiple large basins bounded by basement-cored structural highs (e.g. Gabrielsen, 1984; Doré, 1995; Mattos et al., 2016). This third phase of rifting was also marked by notable across-fault thickening of clastic (growth) strata (Faleide et al., 1993; 2008). The base of the Cenozoic succession is marked by a regional unconformity that separates Cretaceous and Paleogene strata (Faleide et al., 2008). The fourth and last reported rifting phase in the Palaeocene – Eocene is linked to the opening of the Norwegian and Greenland seas (e.g. Eldholm & Thiede, 1980; Faleide et al., 2008; Harishidayat et al., 2015). This phase of rifting coincided with increased magmatic activity, followed by a period of glaciation, uplift and erosion (e.g. Eldholm & Thiede, 1980; Faleide et al., 2008; Harishidayat et al., 2015).

Stratigraphy

The sediments filling the SW Barents Sea basins are dominated by clastic rocks overlying Caledonian crystalline basement (e.g. Doré, 1995; Harishidayat et al., 2015) (Fig. 2). The clastic-dominated succession can be divided into six megasequences (e.g. Glørstad-Clark et al., 2010). The 1st megasequence comprises Late Devonian-Early Carboniferous fluvial deposits at its base and marginal marine deposits towards its top (e.g. Larssen et al., 2002). The 2nd megasequence contains Middle Carboniferous-Late Permian clastics in its lower part and carbonates in its upper part, with occasional evaporites in basinal areas (e.g. Larssen et al., 2002). The very top of the 2nd megasequence is dominated by bioclastic limestones that pass upwards into cherts and siliceous limestones (e.g. Larssen et al., 2002). A subaerial unconformity separates the underlaying Late Paleozoic carbonates from the overlaying Early Triassic-Middle Jurassic of the 3rd megasequence (e.g. Glørstad-Clark et al., 2010). This megasequence boundary marks a transition from carbonate-dominated deposition to siliciclastic-dominated sedimentation. The base of the 3rd megasequence comprises predominantly fine-grained shelf clastics, whereas the rest of the unit is dominated by shallow marine and coastal clastic rocks (e.g. Glørstad-Clark et al., 2010). This megasequence is unconformably overlain by a succession of Late Jurassic to Early Cretaceous marine mudstones and thin sandstones, which together form the 4th megasequence (e.g. Glørstad-Clark et al., 2010). The uppermost, Late Cretaceous part of the 4th megasequence is generally composed of mudstones with thin intervals of limestones and sandstones (Faleide et al., 1984, 1993, 2008; Gabrielsen, 1984; Gabrielsen et al., 2016). The 5th and 6th megasequences are Cenozoic and consist mainly of marine mudstones with minor siltstones and sandstones (Faleide et al., 1984,1993, 2008; Gabrielsen, 1984; Gabrielsen et al., 2016).

From the description above, it is clear that strong mechanical competency contrasts exist throughout the sedimentary succession in the SW Barents Sea, with relatively weak mudstone-rich intervals alternating with relative strong, carbonate- and sandstone-dominated intervals. This is especially clear between the 3rd and 4th megasequences, where the sandstone-rich upper part of the 3rd megasequence passes upwards into the mudstone-dominated base of the 4th megasequence (Fig. 2). These mechanical competency contrasts are important in terms of the formation and evolution of the normal faults and extensional growth folds that form the focus of our study.

Data

We used the Fruholmen 3D seismic reflection data, which was acquired and processed by WesternGeco in 2007 and retrieved from the DISKOS database in late 2019 (https://portal.diskos.cgg.com/whereoil-data/). It is a post-stack time migrated (PSTM) seismic reflection cube that covers an area of c. 533 km^2. The in-lines in this survey are oriented 80° clockwise of north whereas the cross-lines are oriented 170° clockwise of north. The studied fault (TFFC) changes strike within the study area (see below), so we use composite or arbitrary seismic lines, locally oriented normal to strike, to conduct our quantitative analysis of fault structure and throw. The total record length of this survey reaches 5.5 seconds two-way time (TWT). The data were acquired with a group interval of 12.5 meters (m), a shot point interval of 18.75 m and a streamer length of 5000 m. The original sampling interval for this data was 2 milliseconds (ms), which was resampled during data processing to 4 ms. The data was time migrated using Kirchhoff migration, and an amplitude gain was applied at the last stage of the data processing sequence. Full processing report can be accessed from the DISKOS database (https://portal.diskos.cgg.com/whereoil-data/). The data has a dominant frequency of 40 Hz (see supplementary material for complete frequency spectrum) and a vertical resolution over the depth range of interest (c. 1000 m – 3500 m) of c. 12.5 – 25 m, based on an average velocity of 2000 m/s – 4000 m/s derived from sonic log data. This depth interval covers the syn-kinematic stratigraphy and fault-related folds studied here.

In addition to the 3D seismic reflection data, one wellbore (7124/4-1 S) is available in the study area. The wellbore has basic lithostratigraphic data that was retrieved from the Norwegian Petroleum Directorate (http://www.npd.no/en/). However, no checkshot surveys were available from the well to tie it to the seismic reflection data. Furthermore, sonic log data (DT) were available for depths of c. 500 m to the well total depth (2730 m), but other logs, like the density log (RHOB), were only available for depths from c. 1200 m to c. 2700 m. We therefore used a modified seismic-well tie workflow to generate a reliable TDR and to establish an age-constrained seismic-stratigraphic framework for our specific study area (see supplementary materials for a detailed description of our seismic-well tie workflow).

Methods

Seismic interpretation

Our seismic interpretation comprised two main stages. The first stage represented an initial regional interpretation to define the overall basin structure and context of the TFFC, and the second, more detailed stage of interpretation focused around the TFFC towards the southwest part of the study area. During the regional interpretation, we mapped seven key horizons that represented surfaces that mark major changes in seismic facies and represent the top of the acoustic basement (Caledonian?), top Permian-Carboniferous, top Lower Triassic, top Upper Triassic, top Jurassic, top Cretaceous, and base ?Quaternary (Fig. 2). Our detailed interpretation was performed on a cropped seismic volume around the major fault of interest and included 25 horizons that represent two intra-Paleogene, 10 intra-Cretaceous, five intra-Jurassic, and eight intra-Triassic reflections. These detailed interpreted horizons were used in the geometric and kinematic analysis of the fault, in particular the construction of strike-projections (Walsh and Watterson, 1991), and the timing of key periods of fault and fold growth. Given the poor seismic resolution at depth and the lack of well penetrations, it is difficult to distinguish between the 1st and 2nd megasequences, meaning they were combined into one seismic package (Permian – Carboniferous; Fig. 2).

We also used seismic attributes and colour blending techniques to help highlight and map fault networks. First, we used a variance seismic attribute that highlights discontinuities in the seismic signal by returning low values for continuous events and high values for discontinuous events (Randen et al., 2001). Second, we colour blended dip, tensor, and semblance attributes to create a volume that images faults as relatively dark features (for detailed description and definition of these seismic attributes, please refer to Iacopini et al. (2016) and references therein).

Fault kinematic analysis

Our kinematic analysis of the TFFC involves the analysis of strain distribution along and between its constituent segments (e.g. Peacock & Sanderson, 1991; Childs et al., 1995; Childs et al., 2019). In this study, we drew on the methods summarised in Jackson et al. (2017). The first step was to study the temporal and spatial evolution of mapped fault systems from the 3D seismic reflection data using time-structure maps and time-thickness (isochron) maps. Isochron maps note changes in subsidence and accommodation related to fault and fold growth (e.g. Gawthorpe et al., 2003; Morley, 2002; Schlische, 1995; Young et al., 2001; Jackson & Rotevatn, 2013). Isochron map analysis also helps highlight temporal and spatial trends in across-fault thickening, which helps determine fault growth style (e.g. Jackson et al., 2017). Next, we performed throw analysis by creating throw-length (T-x) and throw-depth (T-z) profiles (e.g. Baudon & Cartwright, 2008; Cartwright et al., 1995; Dawers & Anders, 1995; Gupta & Scholz, 2000; Mansfield & Cartwright, 1996; Rykkelid & Fossen, 2002; Jackson & Rotevatn, 2013; Jackson et al., 2017). We collected throw values on composite seismic lines oriented perpendicular to fault strike every c. 150 m. We could then combine the T-x and T-z data to plot and visualise how throw varies across the fault's surface ('strike-projections'; Walsh and Watterson, 1991; see also Duffy et al., 2015). The strike-projections were used to further understand the geometric and kinematic evolution of faults and adjacent folds (e.g. Jackson & Rotevatn, 2013; Jackson et al., 2017; Collanega et al., 2019; Deng & McClay, 2021).

In our study, we measured two types of throw values at each (150 m-spaced) position along the fault (Fig. 3). These were labelled *observed throw* and *projected* throw to denote the difference between values that did or did not include so-called *continuous deformation*, respectively (i.e., folding; Walsh & Watterson, 1991; Walsh et al., 1996; Fig. 3). We could then calculate and display the difference between observed and projected throws to give a measure of the extent and magnitude of folding across the fault surface, given the difference between these values is essentially a proxy for fold amplitude. Throw data collected using so-called *projected horizons* aided in mitigating the local effects of fault scrap erosion, which mainly impacted the post-Triassic succession (Fig. 3).

Results

Structural framework

There are three major fault systems in the study area (Fig. 4a, b). The first one is a basement-involved normal fault system (the TFFC; Fig. 4c). The TFFC strikes NW-SE and dips ENE. However, in the NW corner of the study area, the TFFC strikes E-W and dips N. Based on its relatively large throw (locally >1 km; see below) and the seismic facies of the deepest, seismically imaged material it displaces, the TFFC is likely rooted in crystalline basement rocks. This observation is also confirmed by previous studies using seismic reflection and potential field data (e.g.

Gabrielsen, 1984; Faleide et al., 2008; and Indrevær et al., 2013). The upper tip of the TFFC is typically located within Cretaceous rocks (Figs. 4c and 5). The maximum throw on the TFFC is c. 670 ms (across horizon T5) and c. 1045 ms (across horizon J4) for observed and projected throws, respectively (Fig. 5). When examined closely using seismic attribute time slices, the TFFC appears to be comprised of four distinct geometrical segments (Fig. 4a). These segments are 6-12 km long and have maximum throws that range from c. 339-669 ms and c. 634-1044 ms for observed (across horizon T5) and projected (across horizon J4) throws, respectively.

The second fault system exists in the hanging wall of the TFFC and consists of curvilinear, ENE-WSW striking faults, with lengths of >40 km (Fig. 4a). These faults tend to dip N and die-out to the WSW before linking with the TFFC (Fig. 4a, b). The bottom tip lines of these faults are typically located in the base of the Lower Triassic succession, whereas the upper tip lines are located in uppermost Jurassic-lowermost Cretaceous strata (Fig. 4c). Compared to the TFFC, these E-W striking faults have relatively low throws (c. 40 – 60 ms).

The third fault system is present in the northern part of the study area and consists of numerous relatively short faults (c. 10 – 30 km) that strike NE-SW and dip N-NW (Fig. 4a, b). Similar to the second fault system, these faults have their upper tips located in the Upper Jurassic-Lower Cretaceous strata; however, their basal tips are typically located deeper than those of the second fault system, being located in Lower Triassic-Upper Permian strata (Fig. 4c). The faults in this system tend to have modest throws (up to 200 ms).

Fault-related folding

Fault-parallel folding

Strike-perpendicular seismic sections show extensive deformation of hanging wall strata immediately adjacent to the TFFC (Fig. 5). Folding of Triassic and Jurassic stratigraphic units dominates, defining a fault-parallel hanging wall syncline (Fig. 5a). Underlying Paleozoic stratigraphy and overlying Cretaceous stratigraphy are not or are only very gently folded; Palaeozoic strata are simply offset across the TFFC, whereas Lower Cretaceous strata onlaps onto underlying, folded Jurassic unit (Fig. 5). Along the NW portion of the hanging wall of the TFFC, antithetic and synthetic faults occur, in particular within the gently folded Triassic interval (Fig. 5c, d, f).

Fault-perpendicular folding

We also observe significant fault-perpendicular folding along the TFFC, with major hanging wall synclines and anticlines forming along strike of the fault system (Fig. 6). These large, broad folds are up to 5 km wide and have a maximum amplitude of c. 180 ms (c. 300 m) (Fig. 6). A composite seismic line running parallel to the TFFC shows that the pre-Jurassic succession is tabular, albeit folded. In contrast, the overlying Jurassic interval thins across the anticlines and thickens into the flanking synclines (Fig. 6). However, we cannot clearly see similar thickness changes in the Jurassic sequence on seismic lines trending perpendicular to the fault, a key observation that we return to below (Fig. 5a, b). Towards the NW part of the TFFC, folding is less apparent (Fig. 6). This decrease in folding spatially coincides with an area where the TFFC seems to physically link with the NE-SW fault system (i.e. the third fault system described above; see also Fig. 4a).

Spatial distribution of folding

We can visualise the distribution of folding across and along the fault surface in two ways. The first and simplest way is by looking at folding at specific structural levels (Fig. 7). The second way is by using strike-projections to display how folding varies across the entire fault surface, i.e., areas of enhanced folding are marked by large differences between the observed and projected throw on the strike-projection (Fig. 8). The latter method reveals that the folding along the TFFC seems to be restricted to the sedimentary cover next to the fault and is more prominent in Upper Triassic to Upper Cretaceous strata (Fig. 8c). In detail, there are three distinct areas or patches of folding, which are all greatest at the structural level of the Jurassic (Fig. 8c). Less prominent folding is also observed in the deeper Lower Triassic to Permian-Carboniferous intervals, typically near the centres of the segments comprising the TFFC (Fig. 8c); this is clearly seen in the throw-length plot for the Lower Permian horizon, where the projected and observed throw lines are almost equal along the length of the TFFC (Fig. 7d).

The intensity of folding in the Lower Triassic to Lower Jurassic interval appears to increase towards the NW, with the maximum observed throw difference of c. 300 ms being observed near the centre of fault segment D (Figs. 7b, c and 8c). Whereas both discontinuous and continuous strain appear to generally increase towards the NW (Fig. 8a, b), on the *projected* throw strike-projection we note four clear throw maxima that are spatially linked to and define the centres of the constituent segments of the TFFC (Fig. 8a). In contrast, the *observed* throw strike-projection surface shows only two clear throw maxima that spatially correlate to the centres of segments B and D, and a less prominent throw maximum towards the SE that corresponds to the centre of segment A (Fig. 8b). This is supported by the throw-length plots in Fig. 7, which show that significant changes in throw or fold magnitude correlate with fault branchlines. More specifically, we notice an abrupt degrease in throw magnitude in areas where strain is partitioned between the main fault structure and the intersecting faults (Fig. 8).

The northwesternmost segment of the TFFC (segment D) has notably higher throw than segments to the SE (up to c. 670 ms and c. 1100 ms for observed and projected throws, respectively, compared to c. 500 ms and 700 ms for the other segments; Figs. 5f; 7b-d and 8). A potential explanation for the difference in throw between segment D and other segments in the TFFC is that the throw on the former reflects the combined slip on at least two faults; the TFFC itself, plus a series of physically linked hanging wall splays imaged on the fault attribute slices in Fig. 4a. The impact of splay faulting on these locally high throws becomes clearer when we examine the hanging wall and footwall cut-off points on the strike-projection surfaces (Fig. 8) and the throw-length plots (Fig. 7b-d); on these we can see an increase in the magnitude of folding and fault displacement at fault branchlines. The fact that the NW ends of the TFFC are not imaged within the study area makes it difficult to determine the geometric link between segment D and adjacent structures.

Origin of fault-related folding

Different processes can account for the folding next to the TFFC . First, the folding could be a result of compression. However, this is not the most likely scenario, given the lack of regional evidence for an Early Cretaceous compressional event, and the fact that the observed fold geometries and onlap relationships are not consistent with inversion. The syn-kinematic strata we observe here is not folded and onlaps onto the fault-perpendicular anticlines and onto the steep, basinward dipping limbs of the fault-parallel syncline where with inversion the syn-kinematic strata onlaps onto the inversion fold and early growth strata is folded (e.g. Coleman et al., 2019). Another possible causal mechanism is frictional drag folding (e.g. Schlische, 1995). However, the folds formed along the TFFC are wide (>100s meters), and this is not likely to be the result of drag folding, which typically forms far narrower folds (10s – 100s meters) (Coleman et al., 2019) (Figs. 5a, f and 9a, b). We therefore interpret that the fault-parallel folds are extensional growth folds, formed ahead of the propagating (upper and lower) tips of normal faults (e.g. Withjack et al., 1990; Allmendinger, 1998; Cosgrove & Ameen, 1999; Hardy & McClay, 1999; Gawthorpe & Leeder, 2000; Withjack & Callaway, 2000; Coleman et al., 2019; Jackson et al., 2020). In fact, vertical fault propagation can also produce the frictional drag folds of the type described above, which might be synthetic dip panels (i.e. layers dipping in the same direction) that are remnants of fault tip folding (see Ferrill et al., 2012, 2017 for more details).

Additionally, changes in fault plane geometry might also be responsible for the formation of small-scale fault-perpendicular folds (Ehrlich & Gabrielsen, 2004). For instance, areas where the fault plane is curved (convex or concave) seems to coincide with some of the folding we noted in the Jurassic and Triassic intervals (Fig. 5c-e and 6c). These folds can potentially superimpose smaller structures onto larger ones, or simply augment and amplify the larger structures. However, we interpret the origin of the described fault-perpendicular folds (Fig. 6) to represent now-breached segment boundaries between the lateral tips of precursor faults given their prevalence near the mapped lateral tips of TFFC fault segments (e.g. Gawthorpe et al., 1997; Corfield & Sharp, 2000; Sharp et al., 2000; Willsey et al., 2002; White & Crider, 2006; Kane et al., 2010; Duffy et al., 2013; Khalil & Mcclay, 2017; Tavani et al., 2018; Coleman et al., 2019).

Temporal evolution of the TFFC

Having established the present structural style of the TFFC and described its geometry, we now focus on how this fault system developed through time. We do this by studying thickness variations in syn-kinematic stratal units along and across fault arrays (e.g. Cowie et al., 2000; McLeod et al., 2000; Gawthorpe et al., 2003), as well as the spatial distribution of the fault-related folds described in the previous section; together these observations help us determine the position of now-breached segment boundaries and the style of propagation (surface breaching vs. buried) of the TFFC (e.g. Gawthorpe et al., 1997; Corfield & Sharp, 2000; Sharp et al., 2000). For each interpreted stratigraphic unit, we present our observations first and then provide possible interpretations that could explain how the TFFC might have evolved during that time period.

Carboniferous – Permian (350-250 Ma)

The first seismic package above the crystalline basement is assigned a Carboniferous to Permian age, which makes it lithostratigraphically equivalent to the 1st and 2nd megasequences (Fig. 2). No clear thickness variations are observed across the TFFC during this period (Fig. 10a). However, these Paleozoic strata seems to thicken regionally towards the NE, away from the TFFC, as well as thickening (by c. 70 ms or c. 150 m) across relatively small faults in its footwall (Fig. 10a).

The lack of thickness variations immediately across the TFFC suggests that the fault was not active at this time, although smaller, E-W striking faults in its footwall might have been (Fig. 10a). This style of strain partitioning may have arisen because the smaller faults were more optimally oriented to accommodate N-S-directed stretching associated with this initial period of relatively mild extension (Rift Phase 2; Fig. 2). Regional NE thickening of this seismic package might be related to the long wavelength variations in basin subsidence related to regional tectonic events.

Early Triassic (245-251 Ma)

The second stratal unit is Early Triassic and represents the Klappmyss Formation (Fig. 2). This mudstone-dominated unit is generally well imaged in seismic data and shows no significant thickness variations across the TFFC or across the entire area of interest (Fig. 10b). The only exception to this is the clear across-fault thickening seen in association with the N-dipping fault segments defining the NW portion of the TFFC (e.g. segment D; Figs. 5f and 10b). These thickness variations (up to 200 ms, c. 360 m thick) suggest that these segments were active during this period, while others remained inactive.

Middle Triassic (227-245 Ma)

The third stratal unit is Middle Triassic and represents the Kobbe and Snadd Formations (Figs. 2 and 5c). This unit shows significant thickness variations (43 to 346 ms, c. 80 to 620 m) across all segments of the TFFC, and more minor variations along a NE-trending fault segment located in the NE part of the study area (Figs. 5c and 10c). These thickness variations suggest that segments A, B, C and D of the TFFC, along with a NE-trending fault in its hanging wall, were all active during this period.

Late Triassic (201-227 Ma)

The fourth stratal unit is Late Triassic and represents the Fruholmen Formations (Figs. 2 and 5c). This unit shows thickening across NE- trending fault segment and minor thickness variations across TFFC segments A, B and C (Fig. 10d). In fact, the strata appear to thin towards the TFFC indicating the fault was likely buried during this period (Fig. 10d).

Jurassic (150-200 Ma)

The fourth stratal unit is Jurassic in age and mostly includes the upper part of the 3rd megasequences (Fig. 2). This unit includes all the Jurassic formations and it is well-imaged in seismic data, except for areas immediately next to the TFFC where bedding is relatively steeper and rocks appear highly faulted (Fig. 5c, f). Despite being relatively thin, this unit shows significant thickness variations across and along the TFFC (Fig. 10e). More specifically, we see significant, synclinal depocenters (up to 170 ms, c. 302 m thick) near the centres of all fault segments, with Jurassic strata thinning across and onlapping onto fault-perpendicular anticlines and onto the steeper, basinward-dipping limbs of the fault-parallel syncline (Figs. 9d and 10e). However, the Jurassic stratal unit, having thinned onto the steep dipping limb, then thickens towards the surface of the TFFC (Fig. 9d). The overall across-fault thickening also differs *along strike* of the TFFC, with the maximum across-fault thickening (130 ms or c. 230 m) occurring along segment D (Fig. 10e).

The observed onlap relationships and thickness variations across and along-strike of the TFFC suggest that many of the fault-related folds (i.e., fault-parallel and fault-perpendicular) described above formed during the Early Jurassic (start of Rift Phase 3; Fig. 2). However, this stage of fault-related folding might have been restricted to segments B, C and D of the TFFC, and not segment A. Therefore, we tentatively suggest that segments B, C and D rapidly formed and linked laterally during the Late Triassic to Early Jurassic, before linking to segment A. The fact that the fault-related folding was the prominent at-surface deformation style in the Jurassic, when earlier, during the Triassic, the fault was a surface-breaching structure, requires that the fault was reburied between the Late Triassic to Early Jurassic. Having breached the surface, it is clear from thinning of the footwall strata and the presence of hanging wall depocenters that by the end of the Jurassic, the TFFC was a single, through-going fault system (Fig. 10e).

Cretaceous (97.5-132.6 Ma)

The youngest stratal unit considered is Cretaceous in age and is lithostratigraphically equivalent of the 4th megasequence (Fig. 2). This relatively thick unit (up to 870 ms, c. 1240 m) displays an overall wedge-shaped geometry on seismic data, classically associated with syn-kinematic strata (e.g. Fig. 5a) (Prosser, 1993). However, we further subdivide the unit into three sub-units based on intraformational onlap relationships (Fig. 5). The lowermost sub-unit onlaps onto and thins towards the underlaying Jurassic unit forming the steep, basinward dipping limb of the TFFC hanging wall syncline. The sub-unit is absent in the immediate hanging wall of the fault and from the fault footwall (Figs. 5 and 9). These geometries suggest that the TFFC was acting as a blind, fully linked fault at this stage, leading to fault-propagation folding of cover strata and the formation of an at-surface, basinward-facing monocline (e.g. Sharp et al., 2000) (Figs. 6 and 10f). Having broken surface again during the Jurassic, the fault was reburied such that during the Early Cretaceous the fault was expressed at the surface as a growth fold. In the north of the study, area and in contrast to that seen along the main part of the TFFC, the lower sub-unit thickens across the NE-SW-striking fault branch in the hanging wall of the larger structure (Fig. 10f). Thickening of this sub-unit along the entire strike length of this fault suggests that this was actively accruing displacement as a single, continuous, relatively long structure (c. 35 km) (Fig. 10f).

The middle Cretaceous sub-unit, in comparison to the lowermost one, thickens towards the NE-dipping segments of the TFFC, defining several clear fault-bound depocenters (i.e., A-C), and is partially absent from their footwalls (Fig. 10g). At its base, this sub-unit locally onlaps the underlying, basinward-dipping, lowermost sub-unit; this onlap is not, however, as pronounced as that observed at the base of the lowermost sub-unit where it onlaps onto basinward-tilted Jurassic strata (Figs. 5a-c and 9a-c). The distribution of the uppermost Cretaceous sub-unit time defines several large, fault-bound depocenters, with basal and intraformational onlap towards the TFFC being absent (Figs. 9 and 10h). There is also a notable across-fault thickening along a NE-SW-striking segment that is likely part of the ENE-WSW fault system, as opposed to the TFFC (Figs. 4a and 10h). The presence of discrete fault- rather than fold-bound depocenters in the middle and upper parts of the Cretaceous, as defined by the distribution and seismic-stratigraphic architecture of the related sub-units, suggest that, by this time, the TFFC had breached its overlying fault-related fold to form a classic, half-graben-style depocenter. We interpret that this depocenter was segmented along-strike due to the along-strike variations in accommodation created by differential compaction of underlying strata across earlier-formed (i.e., Triassic and Jurassic) fault-related folds. This is supported by the lack of any clear fault-perpendicular, syncline-anticline pairs along-strike of the TFFC (Fig. 6) and the overall decrease in the throw magnitude at the Cretaceous structural level (Figs. 7a and 8).

Summary

In summary, our temporal evolution model (Fig. 10) suggests that the TFFC was initiated during the Early – Middle Triassic with fault segments B, C and D rapidly forming and linking laterally during the Middle Triassic before linking to segment A. During this period (Middle Triassic), the TFFC was a surface-breaching structure. However, the TFFC was subsequently reburied between the Late Triassic and Early Jurassic forming a fault-related folding deformation style at-surface. By the Late Jurassic the TFFC broke surface again and was a single through-going fault system. The fault was reburied such that during the Early Cretaceous the fault was expressed at the surface as a growth fold. The TFFC breached its overlying fault-related fold to form a classic, half-graben-style depocenter at the time of deposition of the middle and uppermost Cretaceous stratal units. Therefore, the TFFC has experienced two distinct phases of growth folding during its lifetime.

Discussion

Current models show that extensional fault-propagation folds are formed during the early stages of extension, with initially intact monoclines subsequently being breached by their causal faults (e.g. Gawthorpe & Leeder, 2000; Sharp et al., 2000; Jackson & Lewis, 2016; Coleman et al., 2019). Our work on the TFFC shows that the start of growth folding in the area is marked by the thinning and onlap of the Lower Jurassic strata towards the fault onto the NE-dipping limb of the Upper Triassic hanging wall syncline (Figs. 5 and 9). However, a second phase of fault-propagation folding likely occurred during the Early Cretaceous as marked by the onlap of Lower Cretaceous strata onto the underlaying Jurassic unit, and the overall thinning of the Lower Cretaceous towards the TFFC (Figs. 9 and 10f). The thickening of overlying Cretaceous units towards the fault indicates that the fault had breached the fault-propagating fold at this time (Fig. 10g, h). Therefore, the fault-propagation folds we observe did not simply form during the earlier phase of extension, but seemingly are best-developed during the Jurassic and, especially, the Cretaceous, after the fault had been active for some time. In summary, based on our borehole-constrained seismic-stratigraphic framework, our results show that fault-propagation folds can form over periods of c. 25.7 Myr (1st phase of folding) and c. 32 Myr (2nd phase of folding). Multiple phases of superimposed fault-propagation folding can occur if a fault is subsequently reburied

Previous studies have shown that changes in fault dip direction and the presence of multiphase extension results in complex hanging wall fold and fault geometries (Coleman et al., 2019; Deng & McClay, 2019). Our results from the TFFC show that despite the presence of multiphase extension and associated changes in fault geometry as a function of growth patterns, the geometry of the studied extensional growth folds remained relatively simple. This is probably because the area experienced coaxial rifting and did not undergo dramatic changes in extension direction. However, our study confirms the complicated nature of syn-kinematic hanging wall strata and fault geometries as a result of folding before the fault reaches the surface and forms a scarp. The fault propagation folding, and secondary structures observed in the area have led to the formation of complex syn-kinematic hanging wall geometries, with stratal units thinning onto the fold limb and other units thickening towards the fault. These different observed geometries suggest that the nature of syn-kinematic hanging wall strata can be more complex than the classic wedge- shaped cross-sectional geometry often described from extensional basins (e.g. Prosser, 1993).

Differences in host rock rheology, fault propagation rate, and throw magnitude can lead to spatial variability in the size and distribution of growth folds (Mansfield & Cartwright, 2000; Coleman et al., 2019). The fault-propagation folds we studied appear to have preferentially developed above the upper tip line of the TFFC within mechanically weak/incompetent layers (Fig. 8c). As discussed above, the constituent segments of the TFFC fault segments likely linked relatively rapidly during the Late Triassic – Early Jurassic (Figs. 7c and 10d, e). Rapid linkage, which may have been associated with high displacement rates, may account for relatively poor development of fault-propagation folds at the Jurassic structural level (Figs. 5d, f and 6). In contrast, the well-developed Early Cretaceous fault-propagation folds probably reflect a period of relatively low displacement rates on the TFFC. This period of low displacement rates during the Early Cretaceous is consistent with our regional understanding of rift phases as it correlates with very end of Rift Phase 3 (Fig. 2).

Even though the importance of considering ductile deformation when assessing normal fault growth has long been recognized (e.g. Walsh & Watterson, 1991), this notion has only relatively recently seen broader support due to the increasing use of high-quality 3D seismic reflection data and exceptional field exposures that reveal the complex three-dimensional geometry of normal faults and related growth folds (e.g. Childs et al., 2002; Walsh et al., 1999, 2002, 2003; van der Zee & Urai, 2005; Schöpfer et al., 2006; Long & Imber, 2010; Giba et al., 2012; Jackson & Rotevatn, 2013; Duffy et al., 2015; Fossen & Rotevatn, 2016; Conneally et al., 2017; Freitag et al., 2017; Camanni et al., 2019; Jackson et al., 2020; Deng & McClay, 2021). Our study further highlights the value of considering both discontinuous (i.e., faulting) and continuous (i.e., folding) deformation when studying normal fault growth. We show that a significant proportion of strain (10 – 40%; see supplementary material for complete data distribution) on the TFFC is expressed in a ductile manner as (fault-propagation) folding, as opposed to in a brittle manner in the form of shear fracturing or faulting. Therefore, not including the continuous component of the strain field will most likely result in erroneous structural restorations or an incomplete understanding of normal fault growth. Our work on the TFFC also suggests that the construction of strike-projections including both discontinuous and continuous strain, and plotting the difference between the two, can be a quick and powerful tool to illustrate the three-dimensional variability of fault-related folds across normal fault surfaces. When integrated with isochron analysis, this can help us determine the patterns and products of normal fault growth, and the origin and evolution of fault-related folds, both of which have major implications for rift morphology and stratigraphic development.

Conclusions

We used high-quality 3D seismic reflection data from SW Barents Sea, offshore Norway to analyse the along-strike variations and geometric evolution of extensional growth folds associated with a large, basement-involved fault. We showed that this fault system is made of four, now hard-linked segments that are 6-12 km long. Fault-perpendicular anticlines, which are flanked by fault-perpendicular synclines, occur at relict segment boundaries (i.e. displacement-gradient folds), whereas fault-parallel folds (i.e. fault-propagation folds) occur along-strike and down-dip of the flanking fault. Based on the fault-fold relationships and the architecture of the nearby stratigraphic record, we suggest that the fault underwent a phase of relatively rapid lateral linkage in the Late Triassic to Early Jurassic. We also show that fault-propagation folding was protracted (c. 57 Myr), occurring in multiple phases due to periodic burial of the fault by syn- and intra-kinematic strata. Our findings further highlight the value of considering both discrete (i.e., fault-related) and continuous (i.e., fold-related) strain when assessing the processes of fault growth, and the geometry, tectono-stratigraphic evolution, and resource potential of rift basins. Using strike-projections of fault surface is particularly powerful for highlighting 3D variations in faulting and folding, something that may be missed or unclear when using throw-length and throw-depth plots alone.

Acknowledgement

The results presented here are part of Ahmed Alghuraybi's PhD research at Imperial College London, funded by Saudi Aramco. We thank the Norwegian Petroleum Directorate (NPD) for making the seismic and well data publicly available on the Norwegian national data repository for petroleum data (NDR). The Fruholmen 3D seismic reflection dataset can be downloaded from The Diskos NDR (https://portal.diskos.cgg.com/whereoil-data/) by searching for "Fruholmen 3D" and the well data can be found by searching for "7124/4-1 S". We thank Schlumberger for providing access to Petrel software and Geoteric for access to their software. We also thank Amir Joffe, Bailey Lathrop and Sophie Pan from Imperial College's Basins Research Group (BRG) for their input and helpful discussions throughout this research.

Figure Captions

Figure 1. (a) Regional structural elements of SW Barents Sea. The study area is highlighted in yellow. The location of the studies used to further constrain seismic facies and age relationships is noted by S1 (Mohammedyasin et al., 2016) and S2 (Harishidayat et al., 2015 and Torabi et al., 2019). The red dashed line shows the location of the regional 2D cross section shown in Fig 1b. Structural elements abbreviations (FH: Fedynsky High, VD: Veslekari Dome, NB: Nordkapp Basin, NH: Norsel High, SG: Swaen Graben, MH: Mercurius High, SD: Samson Dome, LH: Loppa High, HB: Hammerfest Basin, BF: Bjørnøyrenna Fault Complex, VH: Veslemøy High, SR: Senja Ridge, TFFC: Troms-Finnmark Fault Complex, MF: Måsøy Fault Complex, SB: Sørvestsnaget Basin, SH: Stappen High, BP: Bjarmeland Platform, TB: Tromsø Basin, FB: Finnmark Platform).

The map is modified after information found in the Norwegian Petroleum Directorate fact page http://www.npd.no/en/. (b) Regional 2D seismic cross section showing the basin scale settings across The Finnmark Platform, Hammerfest Basin and Loppa High (modified from Gabrielsen, 1984 and Mohammedyasin et al., 2016).

Figure 2. Stratigraphic column for SW Barents Sea showing major tectonic events (modified after Gac et al., 2018 and Edmundson et al., 2019). The figure shows the major seismic horizons picked in the area and near the well location.

Figure 3. Cartoon illustrations showing Left: how projected and observed throw cut-off points are picked to distinguish between throw due to tectonic subsidence alone and throw due to tectonic subsidence and deformation (modified after Duffy et al., 2015). Right: a degraded fault scrap.

Figure 4. (a) Top: time slice at depth of 1400 ms that reveal the major fault systems in the study area using colour blending that combines tensor (yellow), dip (cyan) and semblance (magenta). Middle: a variance horizon slice extracted at the J5 level that shows the fault segments comprising the TFFC structure. Bottom: interpreted fault systems using seismic attribute data above that shows the three fault systems within the study area. The red dotted line shows the composite seismic line location (Fig 4c). The TFFC fault segments are labeled A-D. (b) Time structure maps of the base Permian-Carboniferous (Top) and base Jurassic (Middle) horizons. These horizons represent base syn-rift surfaces that corresponds to the 2nd and 3rd rift phases. The Blue dashed lines show the location of the seismic sections shown on Figs 4 & 5. The black

dashed area represents the extent of the detailed horizon interpretation used in the fault kinematic analysis and Fig 9. Bottom: interpreted structures from the base-Jurassic horizon. (C) Composite seismic line that highlights the structural variability between the three fault systems in the study area. Faults are colour-coded following the map legend in Fig 4a (Black: TFFC, Blue: E-W fault system, Maroon: ENE-WSW fault system).

Figure 5. Interpreted seismic sections taken perpendicular to the strike of TFFC. These sections show the changes in fault patterns and deformation along the TFFC. Black arrows represent observed reflection terminations and red arrows highlight key onlap relationships in the sedimentary cover approaching the fault surface. The location of these sections is shown on Fig 4b.

Figure 6. (A) Composite seismic line taken along strike of the TFFC. The line location is given in Fig. 4b. Location of seismic sections perpendicular to TFFC (Fig 5) are shown as black dashed lines. TFFC fault segments are labelled A-D and shown above the interpreted composite seismic section (B). Time-structure maps for the P-C4 (1), T4 (2), J4 (3) and C4 (4) horizons are shown below the interpreted composite seismic line to show the fold development and distribution across different structural level.

Figure 7. Throw-length profiles for horizons C4, J4, T4 and P-C4 (Lower Cretaceous, Lower Jurassic, Lower Triassic and Lower Permian of Upper Carboniferous). The blue line represents projected throw values while the red line shows the observe throw values. The difference between the two throw types is shaded in light yellow to represent ductile deformation. TFFC

fault segments are marked by the green lines separating segments A – D from left to right.

Figure 8. Strike-projected throw distributions along the TFFC surface for projected (A) and observed (B) throws. The two strike-projections show increased throw towards the NW part of the fault and local throw maximums along strike of the fault. The location of the local throw maximums coincides with the centre of each fault segment making the TFFC structure. The throw maximum the NW corresponds with a branchline that is interacting with the TFFC. The image on the right (C) shows the throw difference between projected and observed throws and represent the folding component along the TFFC, which is shown to be restricted in the sedimentary cover above basement. TFFC fault segments are marked by the green lines and annotated A – D respectively.

Figure 9. Un-interpreted and interpreted, vertically exaggerated (x10) versions of the seismic sections shown in Fig.5 that highlight the folding and onlap relationships in the U. Triassic – u. Cretaceous stratigraphy.

Figure 10. Isochrone maps (left) and interpretive sketches (right) for key stratigraphic units across the TFFC. The isochrone maps and accompanying sketches illustrate the thickness variations across the stratigraphic unit and constrain the timing of fault activity in the TFFC and adjacent faults. The location of individual TFFC fault segments is marked by the labelled circles A – D.

References

Allmendinger, R. W. (1998). Inverse and forward numerical modeling of trishear fault-propagation folds. Tectonics, 17(4), 640–656.

Baudon, C., & Cartwright, J. (2008). The kinematics of reactivation of normal faults using high resolution throw mapping. Journal of Structural Geology, 30(8), 1072–1084. https://doi.org/10.1016/j.jsg.2008.04.008

Bell, R. E., Jackson, C. A. L., Whipp, P. S., & Clements, B. (2014). Strain migration during multiphase extension: Observations from the northern North Sea. *Tectonics*, *33*(10), 1936–1963. https://doi.org/10.1002/2014TC003551

Camanni, G., Roche, V., Childs, C., Manzocchi, T., Walsh, J., Conneally, J., Saqab, M. M., & Delogkos, E. (2019). The three-dimensional geometry of relay zones within segmented normal faults. *Journal of Structural Geology*, *129*(December 2018), 103895. https://doi.org/10.1016/j.jsg.2019.103895

Cardozo, N. (2008). Trishear in 3D. Algorithms, implementation, and limitations. *Journal of Structural Geology*, *30*(3), 327–340. https://doi.org/10.1016/j.jsg.2007.12.003

Cartwright, J. A., Trudgill, B. D., & Mansfield, C. S. (1995). Fault growth by segment linkage: an explanation for scatter in maximum displacement and trace length data from the Canyonlands Grabens of SE Utah. Journal of Structural Geology, 17(9), 1319–1326. https://doi.org/10.1016/0191-8141(95)00033-A

Childs, C., Walsh, J. J., & Watterson, J. (1997). Complexity in fault zone structure and implications for fault seal prediction. *Norwegian Petroleum Society Special Publications*, *7*(C), 61–72. https://doi.org/10.1016/S0928-8937(97)80007-0

Childs, C., Watterson, J., & Walsh, J. J. (1995). Fault overlap zones within developing normal fault systems. *Journal - Geological Society (London)*, *152*(3), 535–549. https://doi.org/10.1144/gsjgs.152.3.0535

Childs, Conrad, Holdsworth, R. E., Jackson, C. A. L., Manzocchi, T., Walsh, J. J., & Yielding, G. (2017). Introduction to the geometry and growth of normal faults. *Geological Society Special Publication*, *439*(1), 1–9. https://doi.org/10.1144/SP439.24

Childs, Conrad, Nicol, A., Walsh, J. J., & Watterson, J. (2002). The growth and propagation of synsedimentary faults. *Journal of Structural Geology*, *25*(4), 633–648. https://doi.org/10.1016/S0191-8141(02)00054-8

Childs, Conrad, Worthington, R. P., Walsh, J. J., & Roche, V. (2019). Conjugate relay zones: geometry of displacement transfer between opposed-dipping normal faults. *Journal of Structural Geology*, *118*(June 2018), 377–390. https://doi.org/10.1016/j.jsg.2018.11.007

Coleman, A. J., Duffy, O. B., & Jackson, C. A. L. (2019). Growth folds above propagating normal faults. *Earth-Science Reviews*, *196*. https://doi.org/10.1016/j.earscirev.2019.102885

Collanega, L., Siuda, K., A.-L. Jackson, C., Bell, R. E., Coleman, A. J., Lenhart, A., Magee, C., & Breda, A. (2019). Normal fault growth influenced by basement fabrics: The importance of preferential nucleation from pre-existing structures. *Basin Research*, *31*(4), 659–687. https://doi.org/10.1111/bre.12327

Conneally, J., Childs, C., & Nicol, A. (2017). Monocline formation during growth of segmented faults in the Taranaki Basin, offshore New Zealand. *Tectonophysics*, *721*(July), 310–321. https://doi.org/10.1016/j.tecto.2017.06.036

Corfield, S., & Sharp, I. R. (2000). Structural style and stratigraphic architecture of fault propagation folding in extensional settings: A seismic example from the Smorbukk area, Halten Terrace, Mid-Norway. *Basin Research*, *12*(3–4), 329–341. https://doi.org/10.1111/j.1365-2117.2000.00133.x

Corfield, Stephen, Sharp, I., Häger, K. O., Dreyer, T., & Underhill, J. (2001). An integrated study of the garn and melke formations (middle to upper jurassic) of the smorbukk area, halten terrace, mid-norway. *Norwegian Petroleum Society Special Publications*, *10*(C), 199–210. https://doi.org/10.1016/S0928-8937(01)80014-X

Cosgrove, J. W., & Ameen, M. S. (1999). A comparison of the geometry, spatial organization and fracture patterns associated with forced folds and buckle folds. Geological Society, London, Special Publications, 169(1), 7 LP – 21. https://doi.org/10.1144/GSL.SP.2000.169.01.02

Cowie, P. A., Gupta, S., & Dawers, N. H. (2000). Implications of fault array evolution for synrift depocentre development: Insights from a numerical fault growth model. *Basin Research*, *12*(3–4), 241–261. https://doi.org/10.1111/j.1365-2117.2000.00126.x

Dawers, N. H., & Anders, M. H. (1995). Displacement-length scaling and fault linkage. Journal of Structural Geology, 17(5), 607–614. https://doi.org/10.1016/0191-8141(94)00091-D

Deng, H., & McClay, K. (2019). Development of extensional fault and fold system: Insights from 3D seismic interpretation of the Enderby Terrace, NW Shelf of Australia. *Marine and Petroleum Geology*, *104*(December 2018), 11–28. https://doi.org/10.1016/j.marpetgeo.2019.03.003

Deng, H., & McClay, K. (2021). Three-dimensional geometry and growth of a basement-involved fault network developed during multiphase extension, Enderby Terrace, North West Shelf of Australia. GSA Bulletin, 1–28. https://doi.org/10.1130/b35779.1

Doré, A. G. (1995). Barents Sea Geology, Petroleum Resources and Commercial Potential. Arctic, 48(3), 207–221. http://www.jstor.org/stable/40511656

Duffy, O. B., Bell, R. E., Jackson, C. A. L., Gawthorpe, R. L., & Whipp, P. S. (2015). Fault growth and interactions in a multiphase rift fault network: Horda Platform, Norwegian North Sea. *Journal of Structural Geology*, *80*, 99–119. https://doi.org/10.1016/j.jsg.2015.08.015

Duffy, O. B., Gawthorpe, R. L., Docherty, M., & Brocklehurst, S. H. (2013). Mobile evaporite controls on the structural style and evolution of rift basins: Danish Central Graben, North Sea. *Basin Research*, *25*(3), 310–330. https://doi.org/10.1111/bre.12000

Ehrlich, R., & Gabrielsen, R. H. (2004). The complexity of a ramp-flat-ramp fault and its effect on hanging-wall structuring: An example from the Njord oil field, offshore mid-Norway. *Petroleum Geoscience*, *10*(4), 305–317. https://doi.org/10.1144/1354-079303-585

Eldholm, O., & Thiede, J. (1980). Cenozoic continental separation between Europe and Greenland. Palaeogeography, Palaeoclimatology, Palaeoecology, 30(C), 243–259.

https://doi.org/10.1016/0031-0182(80)90060-7

Faleide, J. I., Tsikalas, F., Breivik, A. J., Mjelde, R., Ritzmann, O., Engen, Ø., Wilson, J., & Eldholm, O. (2008). Structure and evolution of the continental margin off Norway and the Barents Sea. Episodes, 31(1), 82–91. https://doi.org/10.18814/epiiugs/2008/v31i1/012

Faleide, Jan I., Vågnes, E., & Gudlaugsson, S. T. (1993). Late Mesozoic-Cenozoic evolution of the south-western Barents Sea in a regional rift-shear tectonic setting. *Marine and Petroleum Geology*, *10*(3), 186–214. https://doi.org/10.1016/0264-8172(93)90104-Z

Faleide, Jan Inge, Gudlaugsson, S. T., & Jacquart, G. (1984). Evolution of the western Barents Sea. *Marine and Petroleum Geology*, *1*(2), 70–78. https://doi.org/10.1016/0264-8172(84)90082-5

Ferrill, D. A., Morris, A. P., & McGinnis, R. N. (2012). Extensional fault-propagation folding in mechanically layered rocks: The case against the frictional drag mechanism. *Tectonophysics*, *576–577*, 78–85. https://doi.org/10.1016/j.tecto.2012.05.023

Ferrill, D. A., Morris, A. P., McGinnis, R. N., Smart, K. J., Wigginton, S. S., & Hill, N. J. (2017). Mechanical stratigraphy and normal faulting. *Journal of Structural Geology*, *94*, 275–302. https://doi.org/10.1016/j.jsg.2016.11.010

Fossen, H., & Rotevatn, A. (2016). Fault linkage and relay structures in extensional settings-A review. *Earth-Science Reviews*, *154*, 14–28. https://doi.org/10.1016/j.earscirev.2015.11.014

Freitag, U. A., Sanderson, D. J., Lonergan, L., & Bevan, T. G. (2017). Comparison of upwards splaying and upwards merging segmented normal faults. *Journal of Structural Geology*, *100*, 1–11. https://doi.org/10.1016/j.jsg.2017.05.005

Gabrielsen, R. H. (1984). Long-lived fault zones and their influence on the tectonic development of the southwestern Barents Sea. *Journal of the Geological Society*, *141*(4), 651–662. https://doi.org/10.1144/gsjgs.141.4.0651

Gabrielsen, Roy H., Sokoutis, D., Willingshofer, E., & Faleide, J. I. (2016). Fault linkage across weak layers during extension: An experimental approach with reference to the Hoop Fault Complex of the SW Barents Sea. *Petroleum Geoscience*, *22*(2), 123–135. https://doi.org/10.1144/petgeo2015-029

Gac, S., Hansford, P. A., & Faleide, J. I. (2018). Basin modelling of the SW Barents Sea. *Marine and Petroleum Geology*, *95*(May), 167–187. https://doi.org/10.1016/j.marpetgeo.2018.04.022

Gawthorpe, R. L., & Leeder, M. R. (2000). Tectono-sedimentary evolution of active extensional basins. *Basin Research*, *12*(3–4), 195–218. https://doi.org/10.1111/j.1365-2117.2000.00121.x

Gawthorpe, Rob L., Jackson, C. A. L., Young, M. J., Sharp, I. R., Moustafa, A. R., & Leppard, C. W. (2003). Normal fault growth, displacement localisation and the evolution of normal fault populations: The Hammam Faraun fault block, Suez rift, Egypt. *Journal of Structural Geology*, *25*(6), 883–895. https://doi.org/10.1016/S0191-8141(02)00088-3

Gawthorpe, Rob L., Sharp, I., Underhill, J. R., & Gupta, S. (1997). Linked sequence stratigraphic and structural evolution of propagating normal faults. *Geology*, *25*(9), 795–798. https://doi.org/10.1130/0091-7613(1997)025<0795:LSSASE>2.3.CO;2

Giba, M., Walsh, J. J., & Nicol, A. (2012). Segmentation and growth of an obliquely reactivated normal fault. *Journal of Structural Geology*, *39*, 253–267. https://doi.org/10.1016/j.jsg.2012.01.004

Glørstad-Clark, E., Faleide, J. I., Lundschien, B. A., & Nystuen, J. P. (2010). Triassic seismic sequence stratigraphy and paleogeography of the western Barents Sea area. *Marine and Petroleum Geology*, *27*(7), 1448–1475. https://doi.org/10.1016/j.marpetgeo.2010.02.008

Gupta, A., & Scholz, C. H. (2000). A model of normal fault interaction based on observations and theory. Journal of Structural Geology, 22(7), 865–879. https://doi.org/10.1016/S0191-8141(00)00011-0

Gupta, S., Underbill, J. R., Sharp, I. R., & Gawthorpe, R. L. (1999). Role of fault interactions in controlling synrift sediment dispersal patterns: Miocene, Abu Alaqa Group, Suez Rift, Sinai, Egypt. *Basin Research*, *11*(2), 167–189. https://doi.org/10.1046/j.1365-2117.1999.00300.x

Hardy, S., & McClay, K. (1999). Kinematic modelling of extensional fault-propagation folding. Journal of Structural Geology, 21(7), 695–702. https://doi.org/10.1016/S0191-8141(99)00072-3

Harishidayat, D., Omosanya, K. O., & Johansen, S. E. (2015). 3D seismic interpretation of the depositional morphology of the Middle to Late Triassic fluvial system in Eastern

Hammerfest Basin, Barents Sea. *Marine and Petroleum Geology*, *68*(November 2017), 470–479. https://doi.org/10.1016/j.marpetgeo.2015.09.007

Iacopini, D., Butler, R. W. H., Purves, S., McArdle, N., & De Freslon, N. (2016). Exploring the seismic expression of fault zones in 3D seismic volumes. *Journal of Structural Geology*, *89*, 54–73. https://doi.org/10.1016/j.jsg.2016.05.005

Indrevær, K., Bergh, S. G., Koehl, J. B., Hansen, J. A., Schermer, E. R., & Ingebrigtsen, A. (2013). Post-Caledonian brittle fault zones on the hyperextended SW Barents Sea margin: New insights into onshore and offshore margin architecture. *Norsk Geologisk Tidsskrift*, *93*(3–4), 167–188.

Jackson, C. A.L., & Larsen, E. (2009). Temporal and spatial development of a gravity-driven normal fault array: Middle-Upper Jurassic, South Viking Graben, northern North Sea. *Journal of Structural Geology*, *31*(4), 388–402. https://doi.org/10.1016/j.jsg.2009.01.007

Jackson, Christopher A.L., & Lewis, M. M. (2016). Structural style and evolution of a salt-influenced rift basin margin; the impact of variations in salt composition and the role of polyphase extension. *Basin Research*, *28*(1), 81–102. https://doi.org/10.1111/bre.12099

Jackson, Christopher A.L., & Rotevatn, A. (2013). 3D seismic analysis of the structure and evolution of a salt-influenced normal fault zone: A test of competing fault growth models. *Journal of Structural Geology*, *54*, 215–234. https://doi.org/10.1016/j.jsg.2013.06.012

Jackson, Christopher A.L., Bell, R. E., Rotevatn, A., & Tvedt, A. B. M. (2017). Techniques to determine the kinematics of synsedimentary normal faults and implications for fault growth models. *Geological Society Special Publication*, *439*(1), 187–217. https://doi.org/10.1144/SP439.22

Jackson, Christopher A.L., Whipp, P. S., Gawthorpe, R. L., & Lewis, M. M. (2020). Structure and kinematics of an extensional growth fold, Hadahid Fault System, Suez Rift, Egypt. *Solid Earth*, *11*(3), 1027–1051. https://doi.org/10.5194/se-11-1027-2020

Jackson, J. A. (1987). Active normal faulting and crustal extension. *Geological Society Special Publication*, *28*(28), 3–17. https://doi.org/10.1144/GSL.SP.1987.028.01.02

Johansen, S. E., Ostisty, B. K., Birkeland, Fedorovsky, Y. F., Martirosjan, V. N., Christensen, O. B., Cheredeev, S. I., Ignatenko, E. A., & Margulis, L. S. (1993). Hydrocarbon potential in the Barents Sea region: Play distribution and potential. In Norwegian Petroleum Society Special Publications (Vol. 2, Issue C, pp. 273–320). Elsevier. https://doi.org/10.1016/B978-0-444-88943-0.50024-1

Kane, K. E., Jackson, C. A. L., & Larsen, E. (2010). Normal fault growth and fault-related folding in a salt-influenced rift basin: South Viking Graben, offshore Norway. *Journal of Structural Geology*, *32*(4), 490–506. https://doi.org/10.1016/j.jsg.2010.02.005

Khalil, S. M., & McClay, K. R. (2002). Extensional fault-related folding, northwestern Red Sea, Egypt. *Journal of Structural Geology*, *24*(4), 743–762. https://doi.org/10.1016/S0191-8141(01)00118-3

Khalil, Samir M., & Mcclay, K. R. (2017). 3D geometry and kinematic evolution of extensional fault-related folds, NW Red Sea, Egypt. *Geological Society Special Publication*, *439*(1), 109–

130. https://doi.org/10.1144/SP439.11

Khalil, Samir M., & McClay, K. R. (2018). Extensional fault-related folding in the northwestern red sea, egypt: Segmented fault growth, fault linkages, corner folds and basin evolution. *Geological Society Special Publication*, *476*(1), 49–81. https://doi.org/10.1144/SP476.12

Larssen, G. B., Elvebakk, G., Henriksen, L. B., Nilsson, I., Samuelsberg, T. J., Stemmerik, L., Worsley, D., Kristensen, S. E., & Svånå, T. a. (2002). Upper Palaeozoic lithostratigraphy of the Southern Norwegian Barents Sea. *Norwegian Petroleum Directorate Bulletin*, *9*, 76.

Laubscher, H., 1982. Die Sudostecke des Rheingrabens-ein kinematisches und dyna- misches problem. *Eclogae Geologicae Helvetiae*, 75 (1), 101–116.

Lewis, M. M., Jackson, C. A. L., & Gawthorpe, R. L. (2013). Salt-influenced normal fault growth and forced folding: The Stavanger Fault System, North Sea. *Journal of Structural Geology*, *54*, 156–173. https://doi.org/10.1016/j.jsg.2013.07.015

Lewis, M. M., Jackson, C. A. L., Gawthorpe, R. L., & Whipp, P. S. (2015). Early synrift reservoir development on the flanks of extensional forced folds: A seismic-scale outcrop analog from the Hadahid fault system, Suez rift, Egypt. *AAPG Bulletin*, *99*(6), 985–1012. https://doi.org/10.1306/12011414036

Long, J. J., & Imber, J. (2010). Geometrically coherent continuous deformation in the volume surrounding a seismically imaged normal fault-array. *Journal of Structural Geology*, *32*(2), 222–234. https://doi.org/10.1016/j.jsg.2009.11.009

Mansfield, C. S., & Cartwright, J. A. (1996). High resolution fault displacement mapping from three-dimensional seismic data: Evidence for dip linkage during fault growth. Journal of Structural Geology, 18(2–3), 249–263. https://doi.org/10.1016/S0191-8141(96)80048-4

Mansfield, C. S., & Cartwright, J. A. (2000). Stratal fold patterns adjacent to normal faults: Observations from the Gulf of Mexico. Geological Society Special Publication, 169, 115–128. https://doi.org/10.1144/GSL.SP.2000.169.01.09

Mattos, N. H., Alves, T. M., & Omosanya, K. O. (2016). Crestal fault geometries reveal late halokinesis and collapse of the Samson Dome, Northern Norway: Implications for petroleum systems in the Barents Sea. *Tectonophysics*, *690*, 76–96. https://doi.org/10.1016/j.tecto.2016.04.043

Maurin, J.-C., & Niviere, B. (1999). Extensional forced folding and décollement of the pre-rift series along the Rhine graben and their influence on the geometry of the syn-rift sequences. Geological Society, London, Special Publications, 169(1), 73 LP – 86. https://doi.org/10.1144/GSL.SP.2000.169.01.06

McHarg, S., Elders, C., & Cunneen, J. (2020). Extensional fault-related folding of the North West shelf, Western Australia. AAPG Bulletin, 104(4), 913–938. https://doi.org/10.1306/08301918030

McLeod, A. E., Dawers, N. H., & Underhill, J. R. (2000). The propagation and linkage of normal faults: Insights from the Strathspey-Brent-Stafjord fault array, Northern North Sea. *Basin Research*, *12*(3–4), 263–284. https://doi.org/10.1111/j.1365-2117.2000.00124.x

Michie, E. A. H., Mulrooney, M. J., & Braathen, A. (2021). Fault Interpretation Uncertainties using Seismic Data, and the Effects on Fault Seal Analysis: A Case Study from the Horda Platform, with Implications for CO$_2$ storage. *Solid Earth Discussions*, *2021*, 1–46. https://doi.org/10.5194/se-2021-23

Mohammedyasin, S. M., Lippard, S. J., Omosanya, K. O., Johansen, S. E., & Harishidayat, D. (2016). Deep-seated faults and hydrocarbon leakage in the Snøhvit Gas Field, Hammerfest Basin, Southwestern Barents Sea. Marine and Petroleum Geology, 77, 160–178. https://doi.org/10.1016/j.marpetgeo.2016.06.011

Morley, C. K. (1999). Patterns of displacement along large normal faults: Implications for basin evolution and fault propagation, based on examples from east Africa. *AAPG Bulletin (American Association of Petroleum Geologists)*, *83*(4), 613–634. https://doi.org/10.1306/00aa9c0a-1730-11d7-8645000102c1865d

Morley, C. K. (2002). Evolution of Large Normal Faults: Evidence from Seismic Reflection Data. AAPG Bulletin, 86(6), 961–978. https://doi.org/10.1306/61EEDBFC-173E-11D7-8645000102C1865D

Patton, T. L. (2004). Numerical models of growth-sediment development above an active monocline. *Basin Research*, *16*(1), 25–39. https://doi.org/10.1111/j.1365-2117.2003.00220.x

Peacock, D. C. P. (2002). Propagation, interaction and linkage in normal fault systems. *Earth-Science Reviews*, *58*(1–2), 121–142. https://doi.org/10.1016/S0012-8252(01)00085-X

Peacock, D. C. P., & Sanderson, D. J. (1991). Displacements, segment linkage and relay ramps in normal fault zones. *Journal of Structural Geology*, *13*(6), 721–733. https://doi.org/10.1016/0191-8141(91)90033-F

Prosser, S. (1993). Rift-related linked depositional systems and their seismic expression. Geological Society, London, Special Publications, 71(1), 35 LP – 66.

Randen, T., Pedersen, S. I., & Sønneland, L. (2001). Automatic extraction of fault surfaces from three-dimensional seismic data. *SEG Technical Program Expanded Abstracts*, *20*(1), 551–554. https://doi.org/10.1190/1.1816675

Ritzmann, O., & Faleide, J. I. (2007). Caledonian basement of the western Barents Sea. *Tectonics*, *26*(5), 1–20. https://doi.org/10.1029/2006TC002059

Rykkelid, E., & Fossen, H. (2002). Layer rotation around vertical fault overlap zones: Observations from seismic data, field examples, and physical experiments. Marine and Petroleum Geology, 19(2), 181–192. https://doi.org/10.1016/S0264-8172(02)00007-7

Schlische, R. W. (1992). Structural and stratigraphic development of the Newark extensional basin, eastern North America: evidence for the growth of the basin and its bounding structures. *Geological Society of America Bulletin*, *104*(10), 1246–1263. https://doi.org/10.1130/0016-7606(1992)104<1246:SASDOT>2.3.CO;2

Schlische, R. W. (1995). Geometry and origin of fault-related folds in extensional settings. American Association of Petroleum Geologists Bulletin, 79(11), 1661–1678. https://doi.org/10.1306/7834de4a-1721-11d7-8645000102c1865d

Schöpfer, M. P. J., Childs, C., & Walsh, J. J. (2006). Localisation of normal faults in multilayer sequences. *Journal of Structural Geology*, *28*(5), 816–833. https://doi.org/10.1016/j.jsg.2006.02.003

Sharp, I. R., Gawthorpe, R. L., Underhill, J. R., & Gupta, S. (2000). Fault-propagation folding in extensional settings: Examples of structural style and synrift sedimentary response from the Suez rift, Sinai, Egypt. *Bulletin of the Geological Society of America*, *112*(12), 1877–1899. https://doi.org/10.1130/0016-7606(2000)112<1877:FPFIES>2.0.CO;2

Tavani, S., Balsamo, F., & Granado, P. (2018). Petroleum system in supra-salt strata of extensional forced-folds: A case-study from the Basque-Cantabrian basin (Spain). Marine and Petroleum Geology, 96(June), 315–330. https://doi.org/10.1016/j.marpetgeo.2018.06.008

Taylor, S. K., Nicol, A., & Walsh, J. J. (2008). Displacement loss on growth faults due to sediment compaction. *Journal of Structural Geology*, *30*(3), 394–405. https://doi.org/10.1016/j.jsg.2007.11.006

Torabi, A., Alaei, B., & Libak, A. (2019). Normal fault 3D geometry and displacement revisited: Insights from faults in the Norwegian Barents Sea. Marine and Petroleum Geology, 99(October 2018), 135–155. https://doi.org/10.1016/j.marpetgeo.2018.09.032

van der Zee, W., & Urai, J. L. (2005). Processes of normal fault evolution in a siliciclastic sequence: A case study from Miri, Sarawak, Malaysia. *Journal of Structural Geology*, *27*(12), 2281–2300. https://doi.org/10.1016/j.jsg.2005.07.006

Walsh, J. J., & Watterson, J. (1991). Geometric and kinematic coherence and scale effects of normal fault systems. In: The Geometry of Normal Faults, edidted by: Roberts, A. M., Yielding, G., Freemen, B., Geol. Soc. Lond. Spec. Publ., 186, 157-170, https://doi.org/10.1144/GSL.SP.1991.056.01.13

Walsh, J. J., Bailey, W. R., Childs, C., Nicol, A., & Bonson, C. G. (2003). Formation of segmented normal faults: A 3-D perspective. *Journal of Structural Geology*, *25*(8), 1251–1262. https://doi.org/10.1016/S0191-8141(02)00161-X

Walsh, J. J., Nicol, A., & Childs, C. (2002). An alternative model for the growth of faults. *Journal of Structural Geology*, *24*(11), 1669–1675. https://doi.org/10.1016/S0191-8141(01)00165-1

Walsh, J. J., Watterson, J., Bailey, W. R., & Childs, C. (1999). Fault relays, bends and branch-lines. *Journal of Structural Geology*, *21*(8–9), 1019–1026. https://doi.org/10.1016/S0191-8141(99)00026-7

Walsh, J. J., Watterson, J., Childs, C., & Nicol, A. (1996). Ductile strain effects in the analysis of seismic interpretations of normal fault systems. Geological Society, London, Special Publications, 99(1), 27 LP – 40. https://doi.org/10.1144/GSL.SP.1996.099.01.04

White, I. R., & Crider, J. G. (2006). Extensional fault-propagation folds: mechanical models and observations from the Modoc Plateau, northeastern California. *Journal of Structural Geology*, *28*(7), 1352–1370. https://doi.org/10.1016/j.jsg.2006.03.028

Willsey, S. P., Umhoefer, P. J., & Hilley, G. E. (2002). Early evolution of an extensional monocline by a propagating normal fault: 3D analysis from combined field study and numerical modeling. *Journal of Structural Geology*, *24*(4), 651–669. https://doi.org/10.1016/S0191-8141(01)00120-1

Withjack, M. O., & Callaway, S. (2000). Active normal faulting beneath a salt layer: An experimental study of deformation patterns in the cover sequence. *AAPG Bulletin*, *84*(5), 627–651. https://doi.org/10.1306/c9ebce73-1735-11d7-8645000102c1865d

Withjack, M. O., Henza, A. A., & Schlische, R. W. (2017). Three-dimensional fault geometries and interactions within experimental models of multiphase extension. *AAPG Bulletin*, *101*(11), 1767–1789. https://doi.org/10.1306/02071716090

Withjack, M. O., Olson, J., & Peterson, E. (1990). Experimental models of extensional forced folds. American Association of Petroleum Geologists Bulletin, 74(7), 1038–1054. https://doi.org/10.1306/0c9b23fd-1710-11d7-8645000102c1865d

Young, M. J., Gawthorpe, R. L., & Hardy, S. (2001). Growth and linkage of a segmented normal fault zone; the Late Jurassic Murchison-Statfjord North Fault, Northern North Sea. Journal of Structural Geology, 23(12), 1933–1952. https://doi.org/10.1016/S0191-8141(01)00038-4

(a)

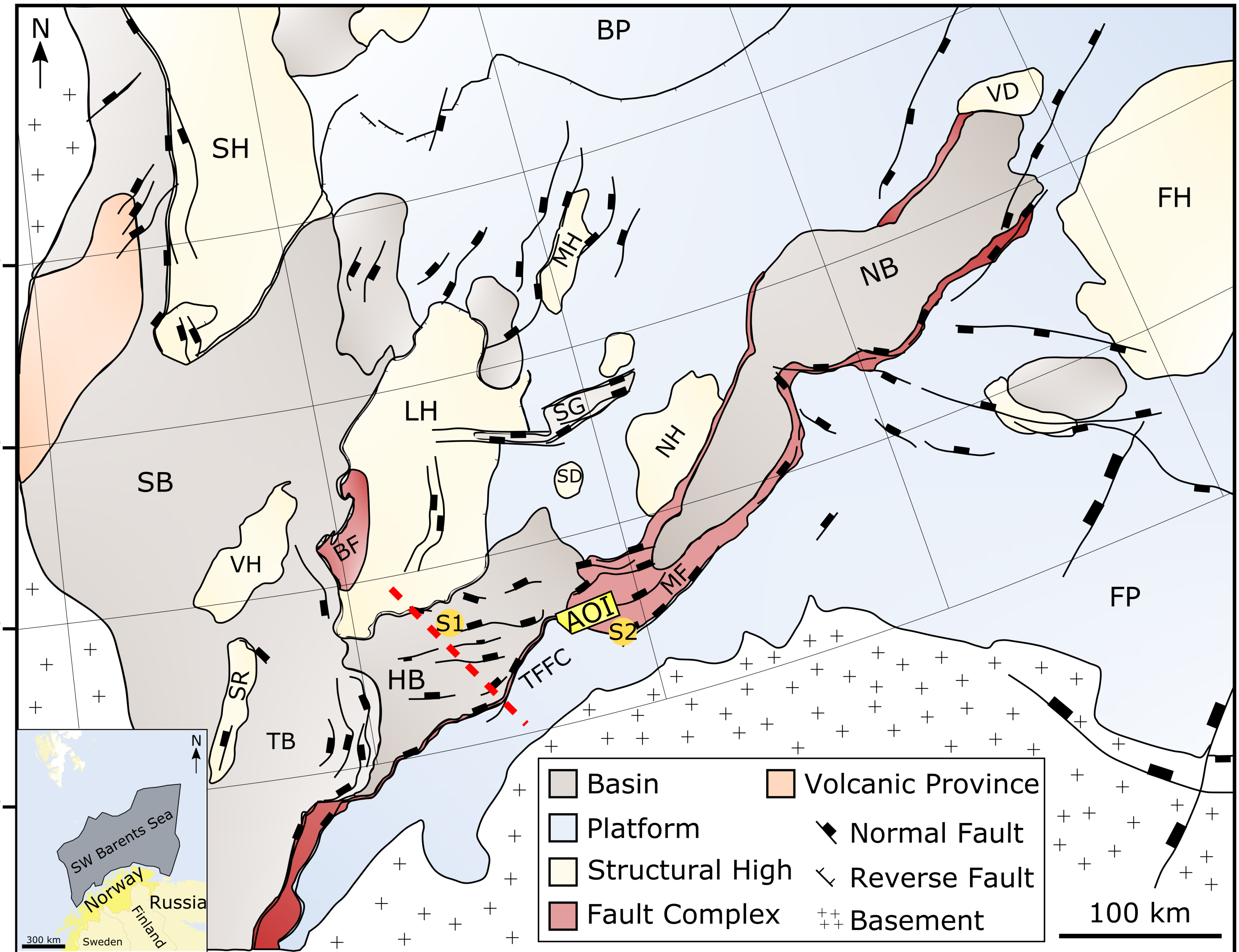

20°
25°
30°
35°
74°
73°
72°
71°
N
BP
SH
VD
FH
MH
NB
LH
SG
NH
SD
SB
BF
VH
MF
FP
AOI
S1
S2
SR
HB
TFFC
TB
SW Barents Sea
Norway
Russia
Finland
Sweden
300 km
Basin
Platform
Structural High
Fault Complex
Volcanic Province
Normal Fault
Reverse Fault
Basement
100 km

Figure 1. (a) Regional structural elements of SW Barents Sea. The study area is highlighted in yellow. The location of the studies used to further constrain seismic facies and age relationships is noted by S1 (Mohammedyasin et al., 2016) and S2 (Harishidayat et al., 2015 and Torabi et al., 2019). The red dashed line shows the location of the regional 2D cross section shown in Fig 1b. Structural elements abbreviations (FH: Fedynsky High, VD: Veslekari Dome, NB: Nordkapp Basin, NH: Norsel High, SG: Swaen Graben, MH: Mercurius High, SD: Samson Dome, LH: Loppa High, HB: Hammerfest Basin, BF: Bjørnøyrenna Fault Complex, VH: Veslemøy High, SR: Senja Ridge, TFFC: Troms-Finnmark Fault Complex, MF: Måsøy Fault Complex, SB: Sørvestsnaget Basin, SH: Stappen High, BP: Bjarmeland Platform, TB: Tromsø Basin, FB: Finnmark Platform). The map is modified after information found in the Norwegian Petroleum Directorate fact page http://www.npd.no/en/. (b) Regional 2D seismic cross section showing the basin scale settings across The Finnmark Platform, Hammerfest Basin and Loppa High (modified from Gabrielsen, 1984 and Mohammedyasin et al., 2016).

(b)

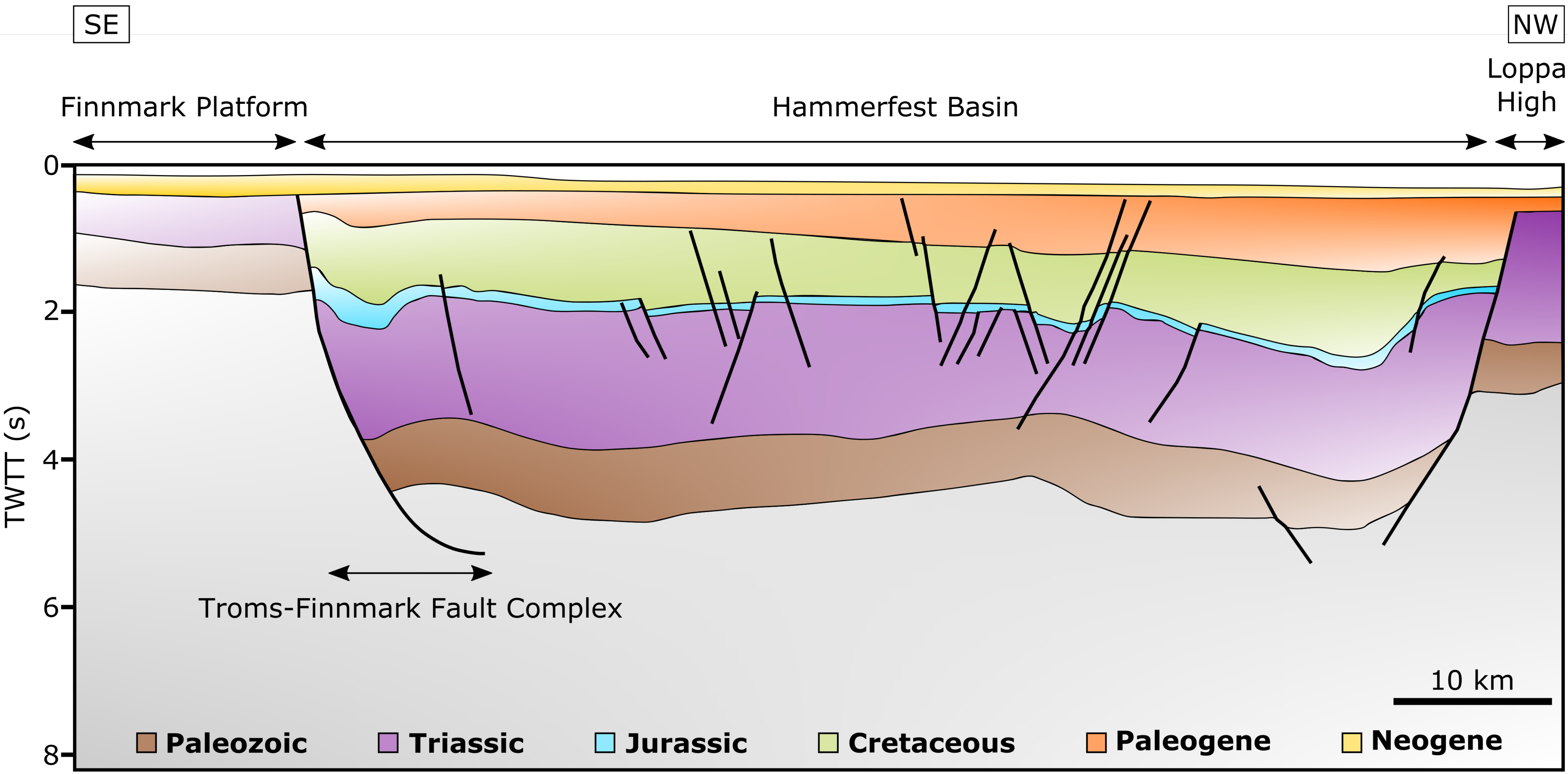

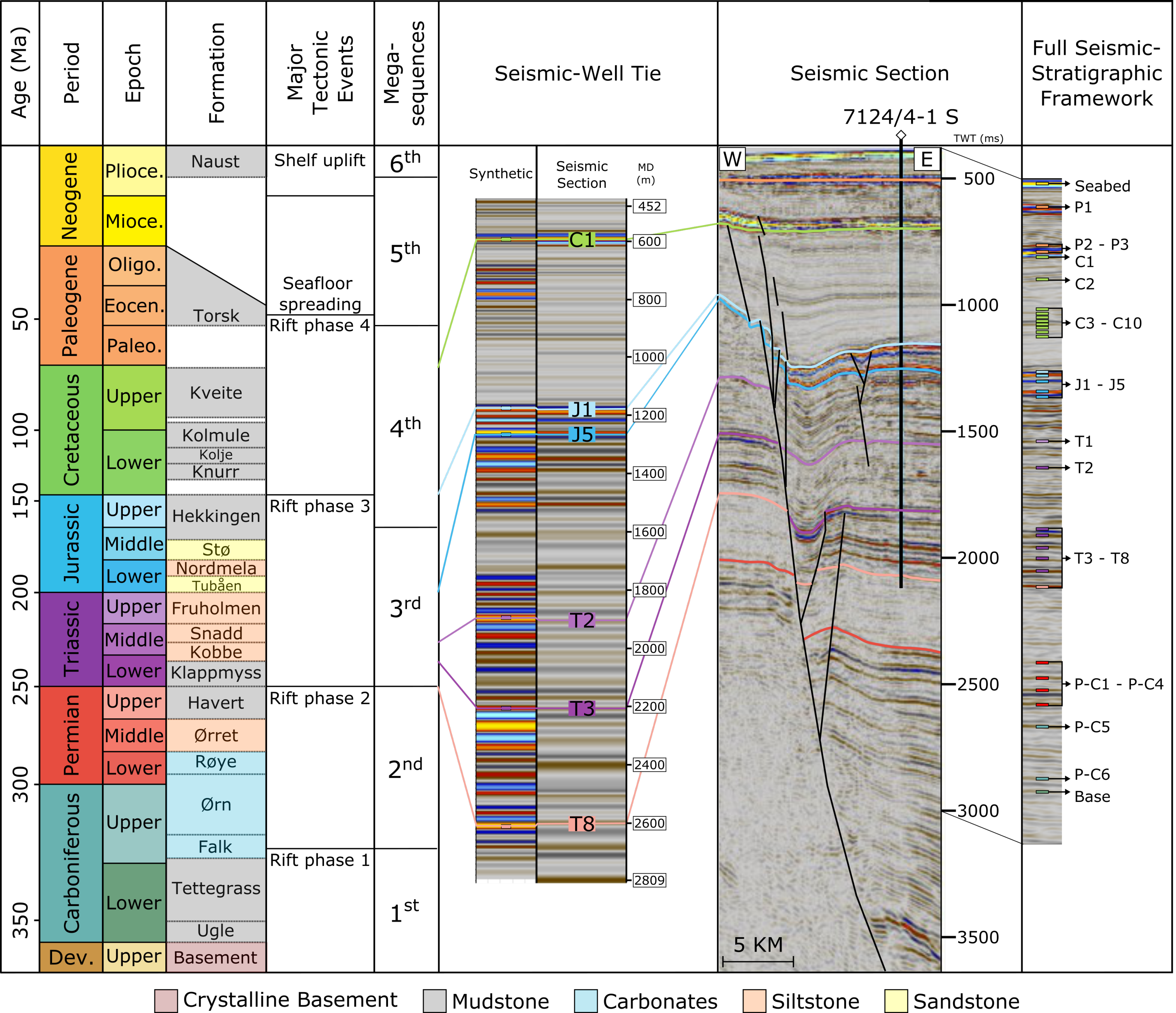

Figure 2. Stratigraphic column for SW Barents Sea showing major tectonic events (modified after Gac et al., 2018 and Edmundson et al., 2019). The figure shows the major seismic horizons picked in the area and near the well location.

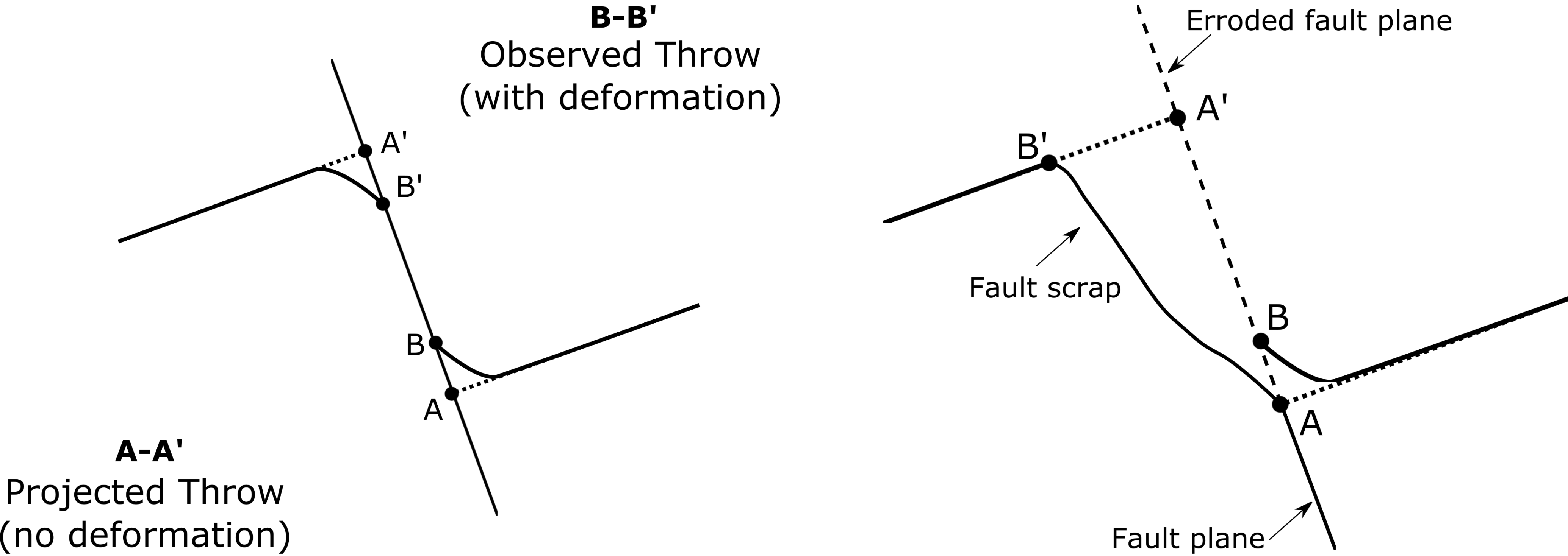

Figure 3. Cartoon illustrations showing Left: how projected and observed throw cut-off points are picked to distinguish between throw due to tectonic subsidence alone and throw due to tectonic subsidence and deformation (modified after Duffy et al., 2015). Right: a degraded fault scrap.

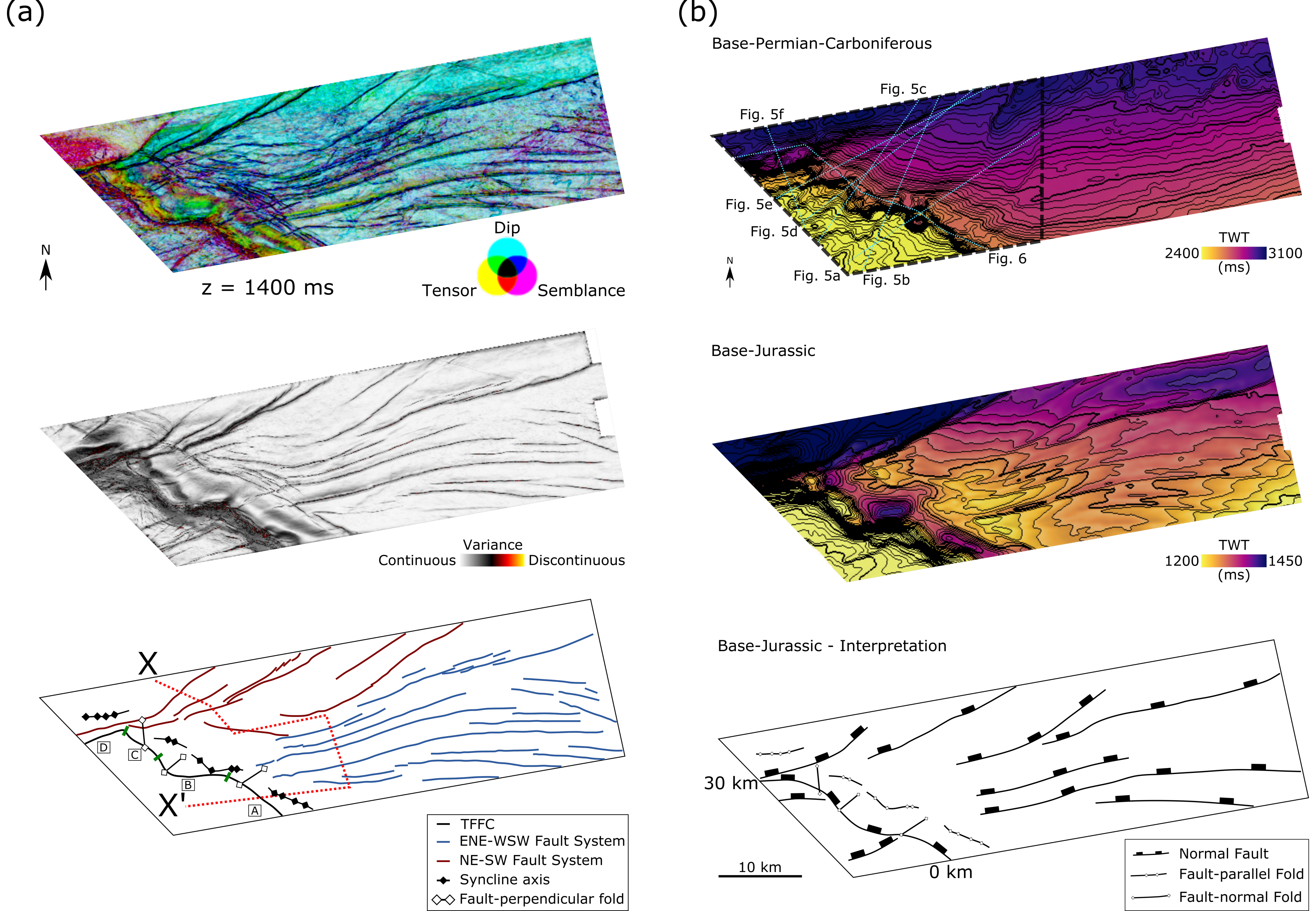
(a)
N
z = 1400 ms
Dip
Tensor
Semblance
Variance
Continuous
Discontinuous
X
X'
A
B
C
D
TFFC
ENE-WSW Fault System
NE-SW Fault System
Syncline axis
Fault-perpendicular fold
(b)
Base-Permian-Carboniferous
Fig. 5c
Fig. 5f
Fig. 5e
Fig. 5d
Fig. 5a
Fig. 5b
Fig. 6
N
TWT
2400
3100
(ms)
Base-Jurassic
TWT
1200
1450
(ms)
Base-Jurassic - Interpretation
30 km
10 km
0 km
Normal Fault
Fault-parallel Fold
Fault-normal Fold

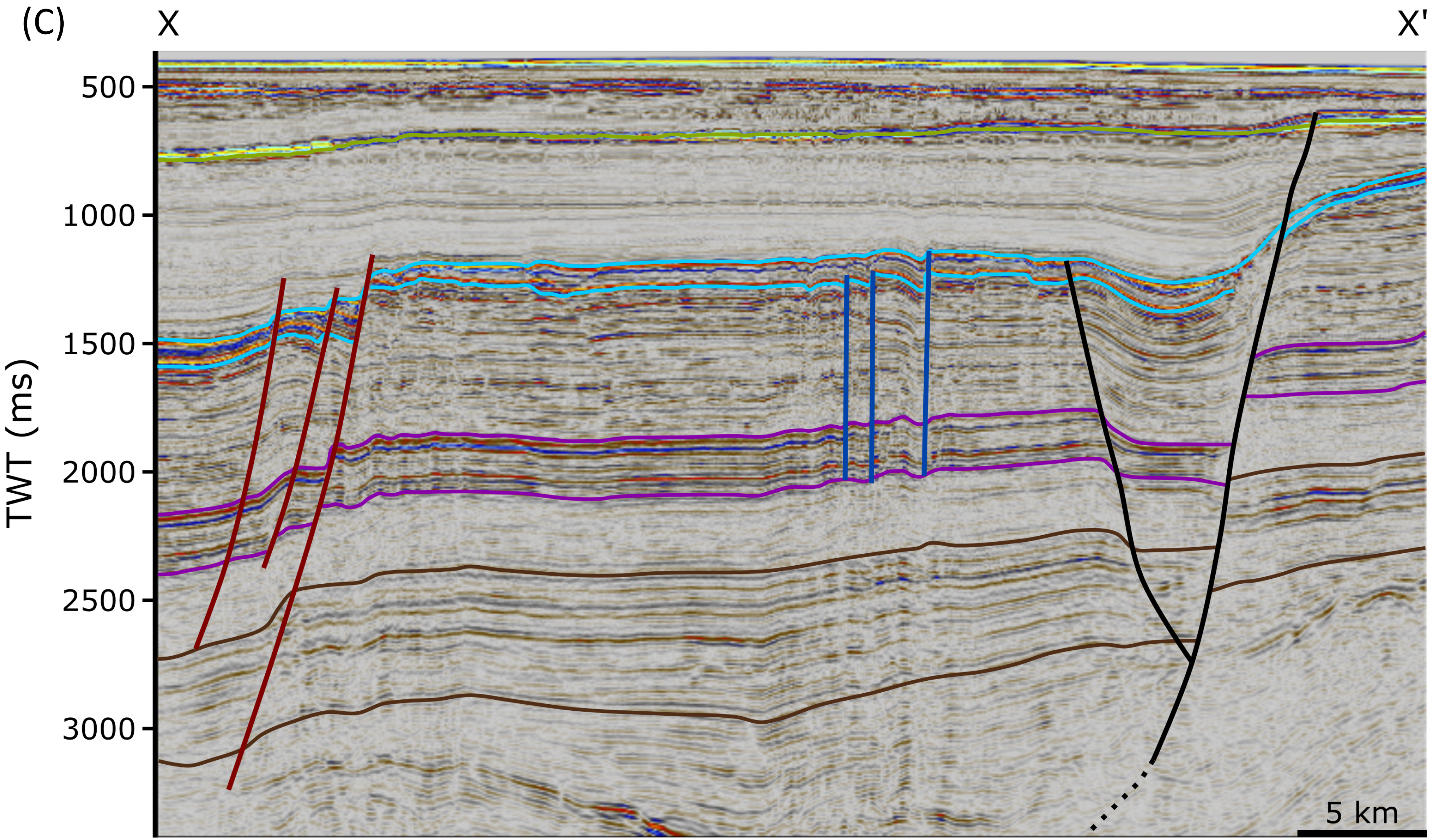

Figure 4. (a) Top: time slice at depth of 1400 ms that reveal the major fault systems in the study area using colour blending that combines tensor (yellow), dip (cyan) and semblance (magenta). Middle: a variance horizon slice extracted at the J5 level that shows the fault segments comprising the TFFC structure. Bottom: interpreted fault systems using seismic attribute data above that shows the three fault systems within the study area. The red dotted line shows the composite seismic line location (Fig 4c). The TFFC fault segments are labeled A-D. (b) Time structure maps of the base Permian-Carboniferous (Top) and base Jurassic (Middle) horizons. These horizons represent base syn-rift surfaces that corresponds to the 2nd and 3rd rift phases. The Blue dashed lines show the location of the seismic sections shown on Figs 4 & 5. The black dashed area represents the extent of the detailed horizon interpretation used in the fault kinematic analysis and Fig 9. Bottom: interpreted structures from the base-Jurassic horizon. (C) Composite seismic line that highlights the structural variability between the three fault systems in the study area. Faults are colour-coded following the map legend in Fig 4a (Black: TFFC, Blue: E-W fault system, Maroon: ENE-WSW fault system).

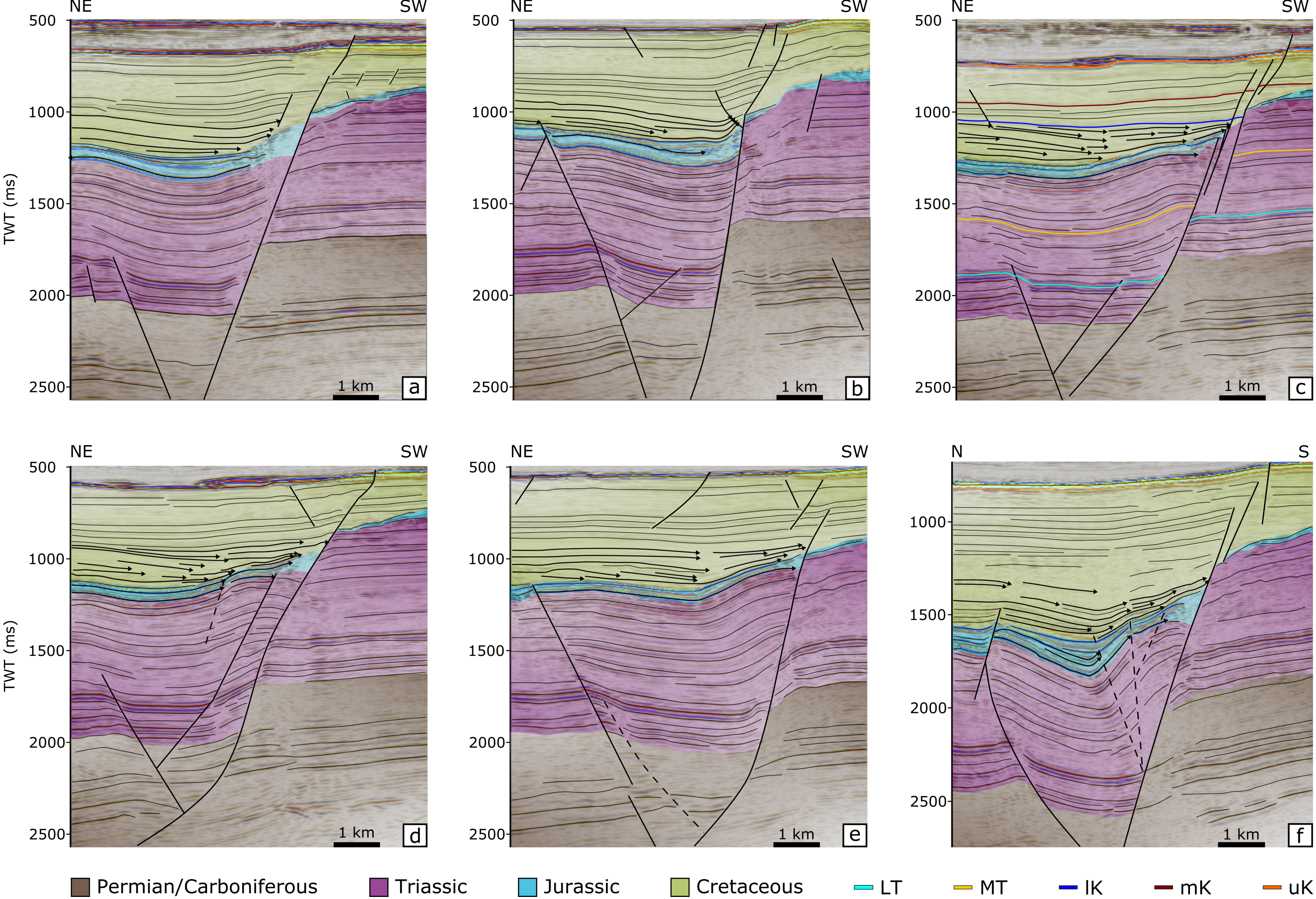

Figure 5. Interpreted seismic sections taken perpendicular to the strike of TFFC. These section show the changes in fault patterns and deformation along the TFFC. Black arrows represent observed reflection terminations and red arrows highlight key onlap relationships in the sedimentary cover approaching the fault surface. The location of these sections is shown on Fig 4b.

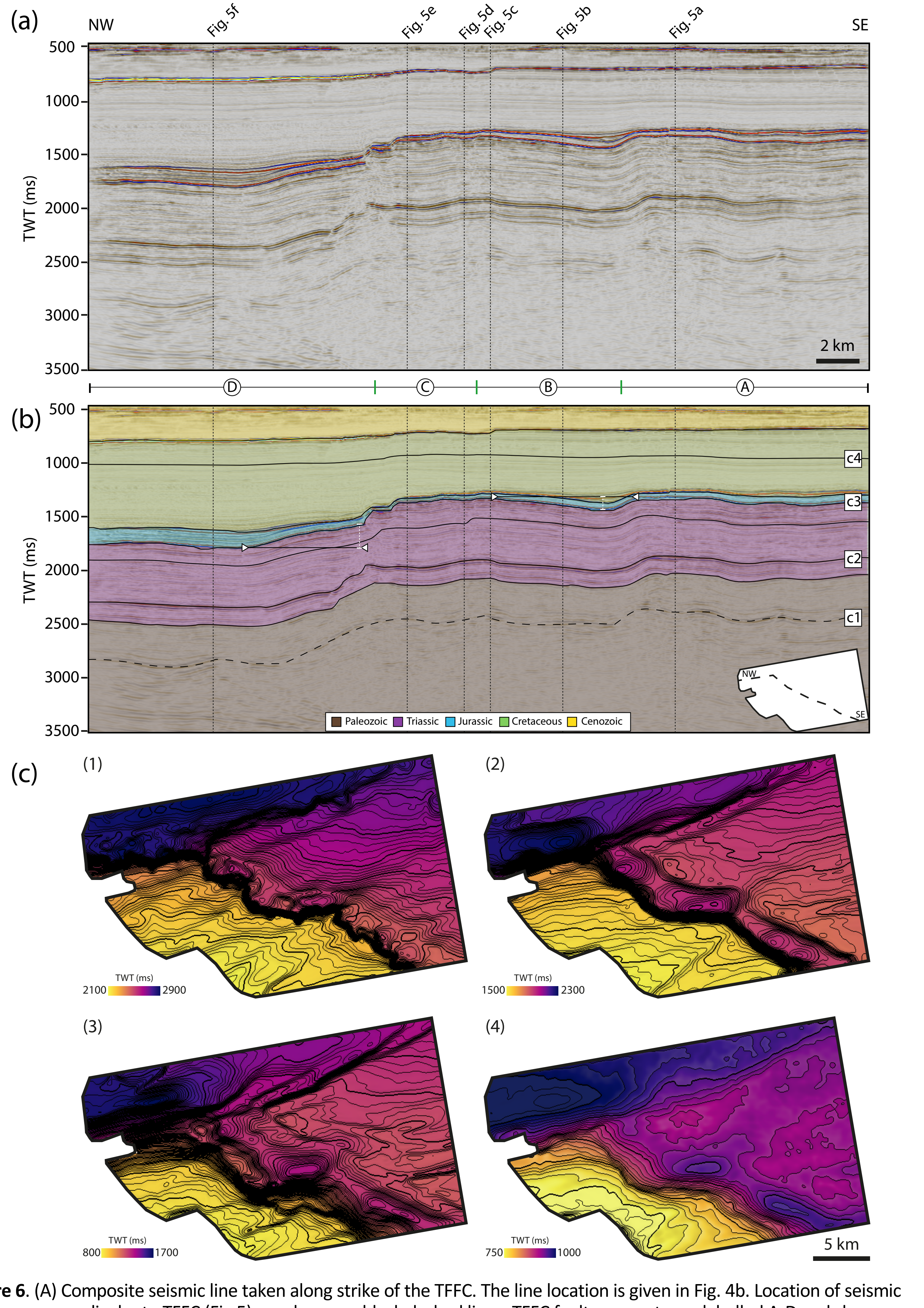

Figure 6. (A) Composite seismic line taken along strike of the TFFC. The line location is given in Fig. 4b. Location of seismic sections perpendicular to TFFC (Fig 5) are shown as black dashed lines. TFFC fault segments are labelled A-D and shown above the interpreted composite seismic section (B). Time-structure maps for the P-C4 (1), T4 (2), J4 (3) and C4 (4) horizons are shown below the interpreted composite seismic line to show the fold development and distribution across different structural level.

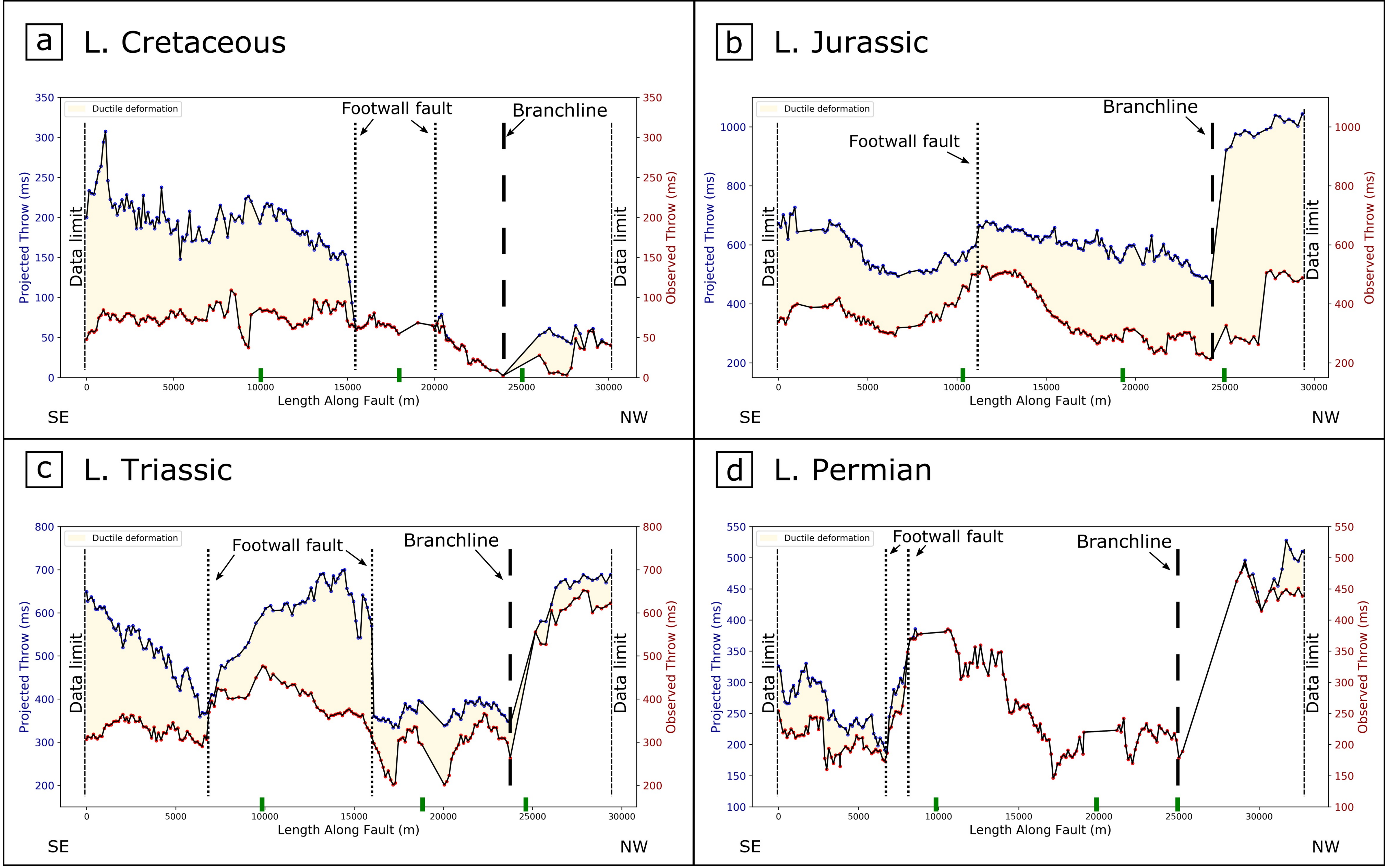

Figure 7. Throw-length profiles for horizons C4, J4, T4 and P-C4 (Lower Cretaceous, Lower Jurassic, Lower Triassic and Lower Permian of Upper Carboniferous). The blue line represents projected throw values while the red line shows the observe throw values. The difference between the two throw types is shaded in light yellow to represent ductile deformation. TFFC fault segments are marked by the green lines separating segments A – D from left to right.

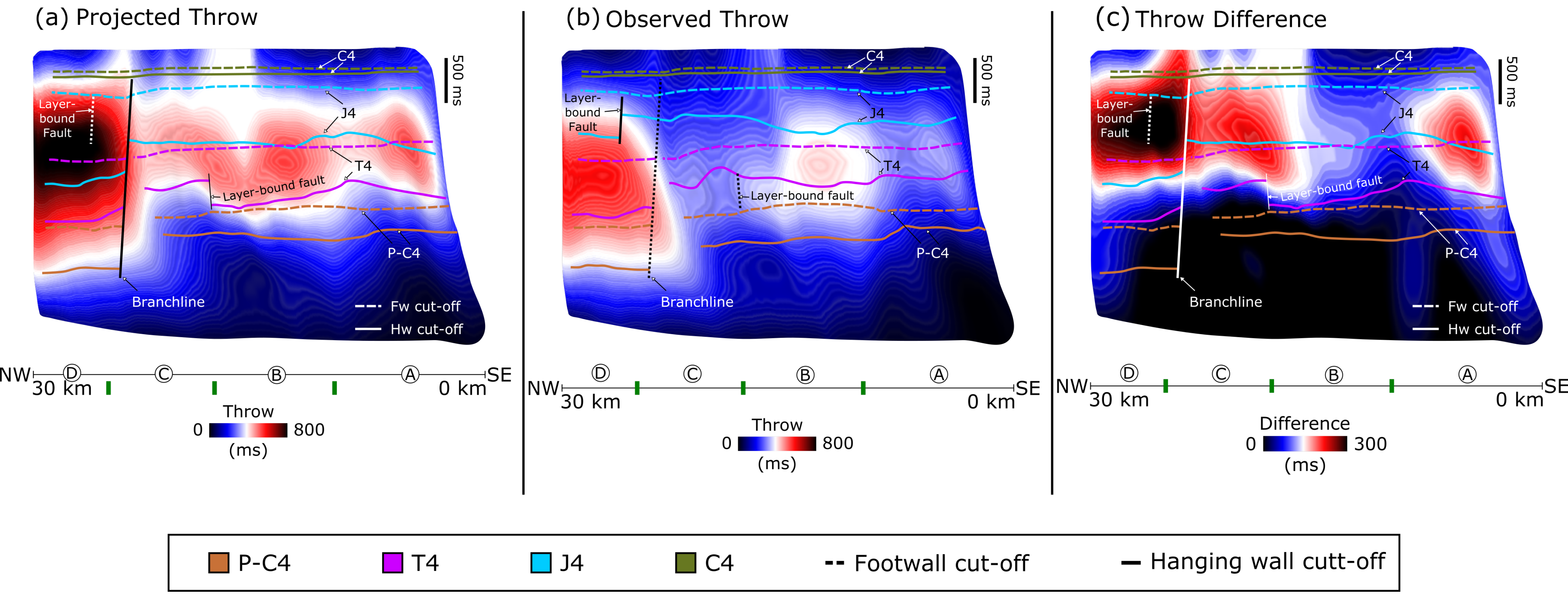

Figure 8. Strike-projected throw distributions along the TFFC surface for projected (A) and observed (B) throws. The two strike-projections show increased throw towards the NW part of the fault and local throw maximums along strike of the fault. The location of the local throw maximums coincides with the center of each fault segment making the TFFC structure. The throw maximum the NW corresponds with a branchline that is interacting with the TFFC. The image on the right (C) shows the throw difference between projected and observed throws and represent the folding component along the TFFC, which is shown to be restricted in the sedimentary cover above basement. TFFC fault segments are marked by the green lines and annotated A – D respectively.

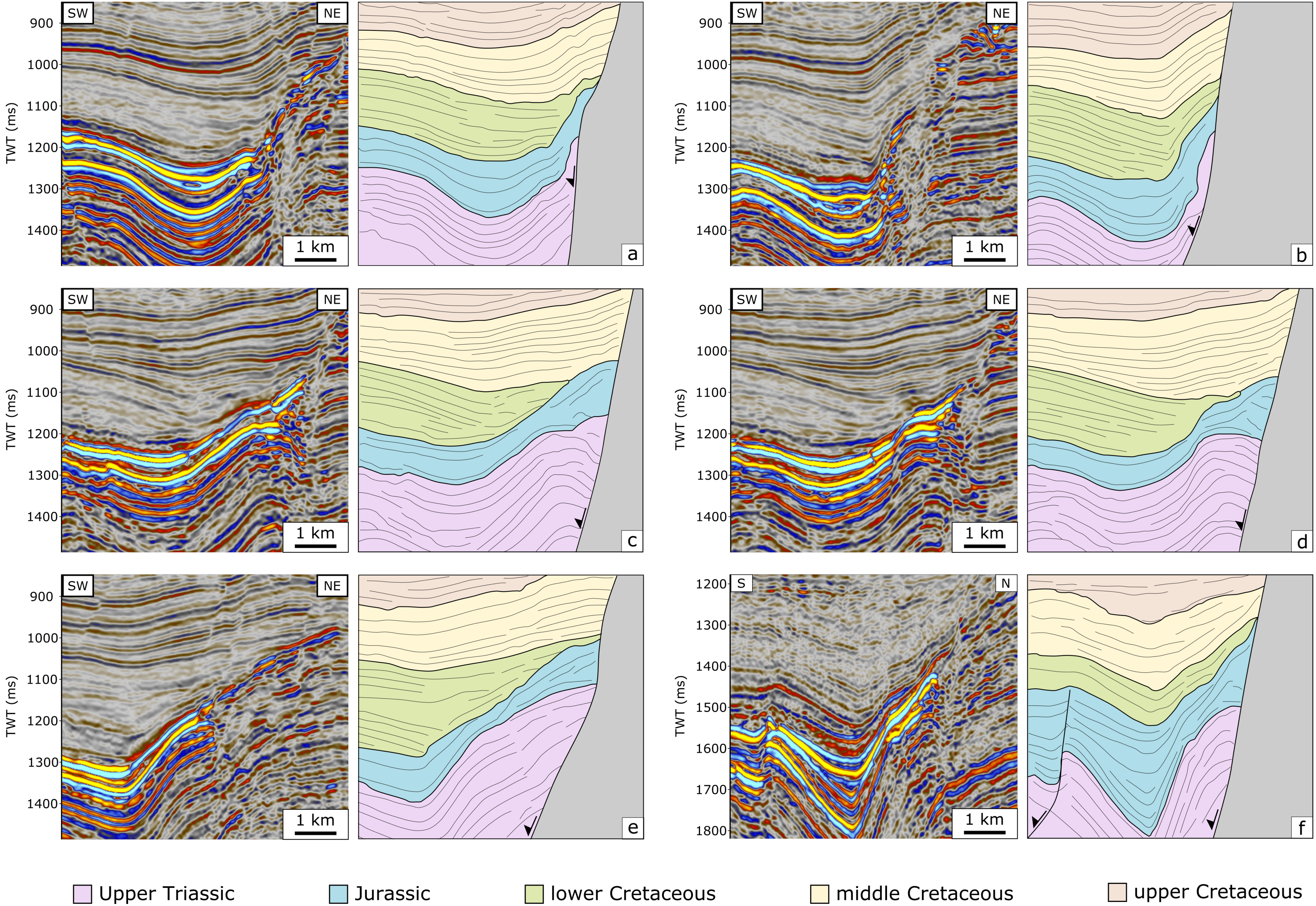

Figure 9. Un-interpreted and interpreted, vertically exaggerated (x10) versions of the seismic sections shown in Fig.5 that highlight the folding and onlap relationships in the U. Triassic – u. Cretaceous stratigraphy.

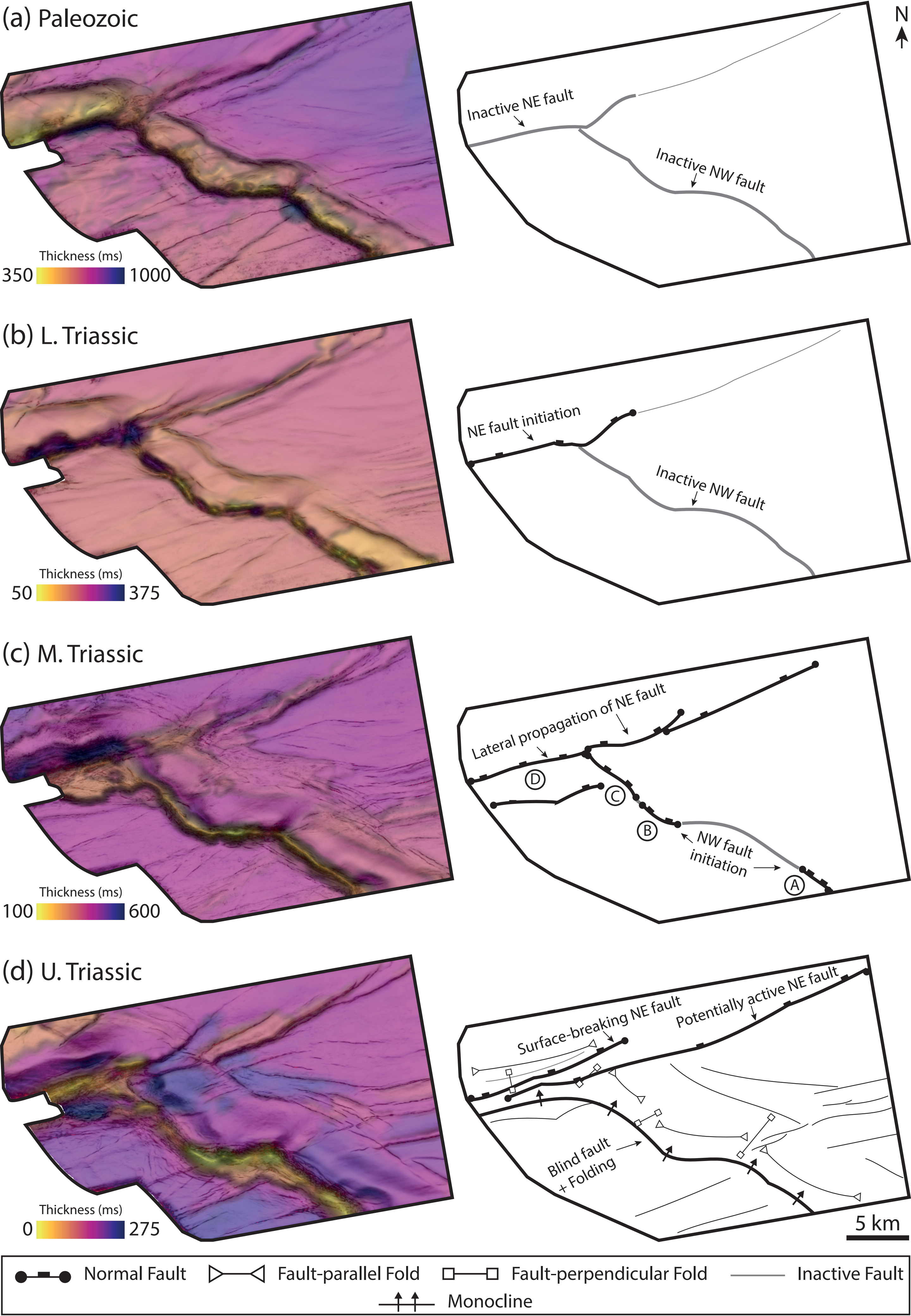
(a) Paleozoic
Thickness (ms)
350
1000
N
Inactive NE fault
Inactive NW fault
(b) L. Triassic
Thickness (ms)
50
375
NE fault initiation
Inactive NW fault
(c) M. Triassic
Thickness (ms)
100
600
Lateral propagation of NE fault
D
C
B
A
NW fault initiation
(d) U. Triassic
Thickness (ms)
0
275
Surface-breaking NE fault
Potentially active NE fault
Blind fault + Folding
5 km
Normal Fault
Fault-parallel Fold
Fault-perpendicular Fold
Inactive Fault
Monocline

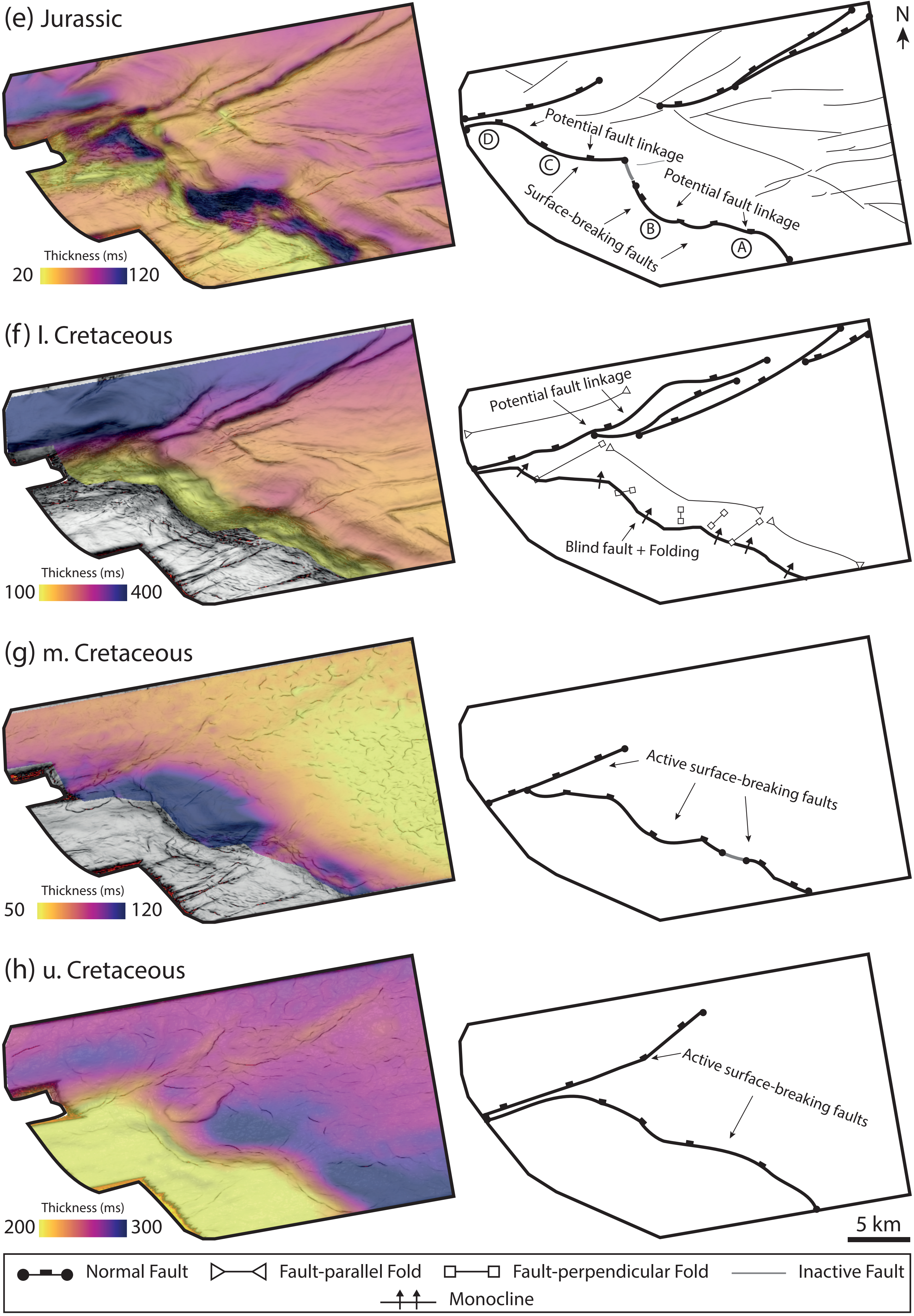

Figure 10. Isochrone maps (left) and interpretive sketches (right) for key stratigraphic units across the TFFC. The isochrone maps and accompanying sketches illustrate the thickness variations across the stratigraphic unit and constrain the timing of fault activity in the TFFC and adjacent faults. The location of individual TFFC fault segments is marked by the labelled circles A – D.

Seismic well tie workflow

In this study, we have a 3D seismic reflection survey and one wellbore. The wellbore has available wireline logs that include density and sonic logs that can be used for seismic well tie. The sonic log data cover a depth interval of c.440 m to total depth (2730 m). While the density log data were measured from c. 1200 m to c. 2700 m (Fig 2). However, the wellbore data did not include any checkshot data or a time depth relationship. Therefore, we followed the workflow described next to establish a time depth relationship between the wellbore and seismic reflection data at the well location.

The first step we did was to interpret key horizons in our seismic data that marked major changes in seismic facies or character. Table.1 shows a summary of the interpreted seismic facies and a description for each unit. Next, we performed a qualitative seismic stratigraphic correlation with offset wells from nearby studies, where we tried to correlate major seismic units based on their overall attributes (i.e., amplitude strength, frequency, lateral continuity and geometry of reflectors). These studies are Harishidayat et al. (2015), Mohammedyasin et al. (2016) and Torabi et al. (2019). Wellbore 7125/4-2 used in Harishidayat et al. (2015) and Torabi et al. (2019) is located c. 34 km SE of our study area while wellbore 7121/4-1 from Mohammedyasin (2016) is situated c. 104 km away towards the west. Representative seismic sections used for this correlation are shown in Fig 3.

After establishing a seismic stratigraphic correlation with offset wells, we proceeded to determine a time-depth relationship at the wellbore location in our study area and calculate a pseudo seismic velocity log. This served as a first iteration towards constraining the age relationships in our study area and reaching a reliable seismic-well tie. We only used this pseudo velocity log as a comparative measure for other velocity estimates to make sure that we are using reasonable values and not completely off with our estimations. The second step we took was to generate a simplified layer cake velocity model using our key seismic surfaces that represented the top of each key seismic unit along with interval velocity values calculated from the average sonic log response the corresponds with each seismic unit. Where sonic log data are missing, we used geologically reasonable seismic velocity estimates that accounted for lithology and depth. From this velocity model, we derived a second time-depth relationship. We also calculated a third time-depth relationship using the previous approach but after applying a median filter to the sonic log data to remove any outlier data points. Together, these velocity modelling steps resulted in two time-depth relationships that we later used as pseudo checkshot data in the seismic-well tie process together with a reference time-depth relationship that was calculated from offset wells and used as a quality check measure.

We followed a two-step workflow to perform the seismic-well tie at the wellbore location in our study area. First, we applied a median filter to the density log data to remove any spikes or outlier data points. Then, we used the filtered density and sonic logs to generate a synthetic seismogram, which we combined with the time-depth relationship (derived from the filtered sonic log data) to tie the well tops to the seismic data. Given the limited coverage of the density log compared to the sonic log, this seismic-well tie step could only tie the well tops from c. 1200 m (Top Hekkingen Formation) to c. 2600 m (Top Havert Formation). Nonetheless, this was a useful step to get a more accurate time-depth relationship that is well-constrained for those deeper horizons. The second step in our efforts to get a reliable seismic-well tie at our area of interest was to use the time-depth relationship from the last step and combine it with a synthetic seismogram that was generated from sonic log data and a computed density log using sonic log data to perform a final seismic-well tie. This newly generated synthetic seismogram can be used to tie the shallower well tops (c. 440 m) in addition to the deeper well tops that were covered by the first seismic-well tie step.

As a result of this iterative velocity modelling and seismic-well tie method, we were able to tie all available well tops to our seismic data using a well-constrained time-depth relationship that integrates all available data. Lastly, to close the loop and increase our confidence with the seismic-well tie, we compared the final seismic-well tie results that were derived completely from our available data to offset wells from the nearby studies.

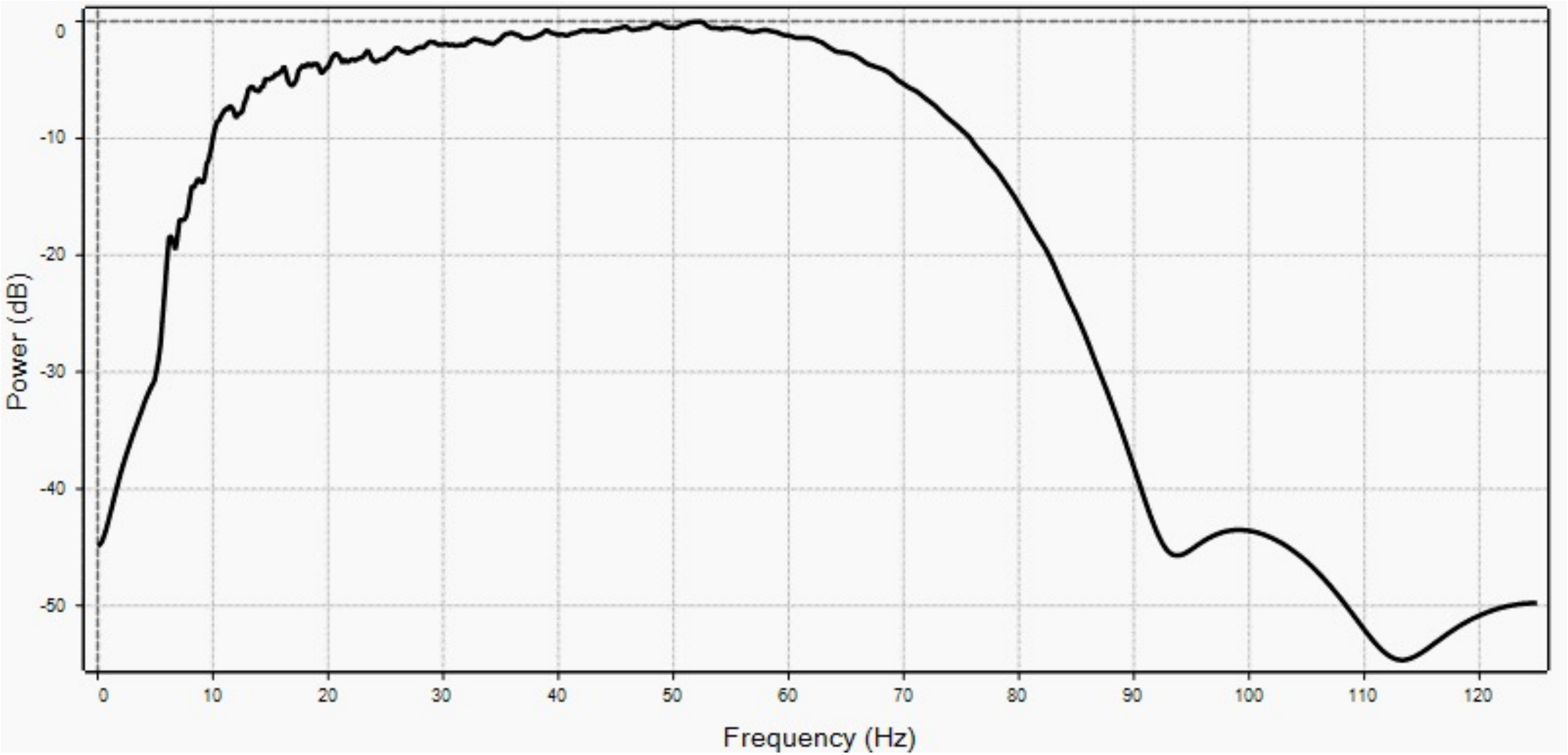

Figure 1. Frequency spectrum for the 3D seismic reflection dataset used in this study. The figure shows that the dominant frequency ranges between 40 – 60 Hz depending on the depth interval within the seismic survey.

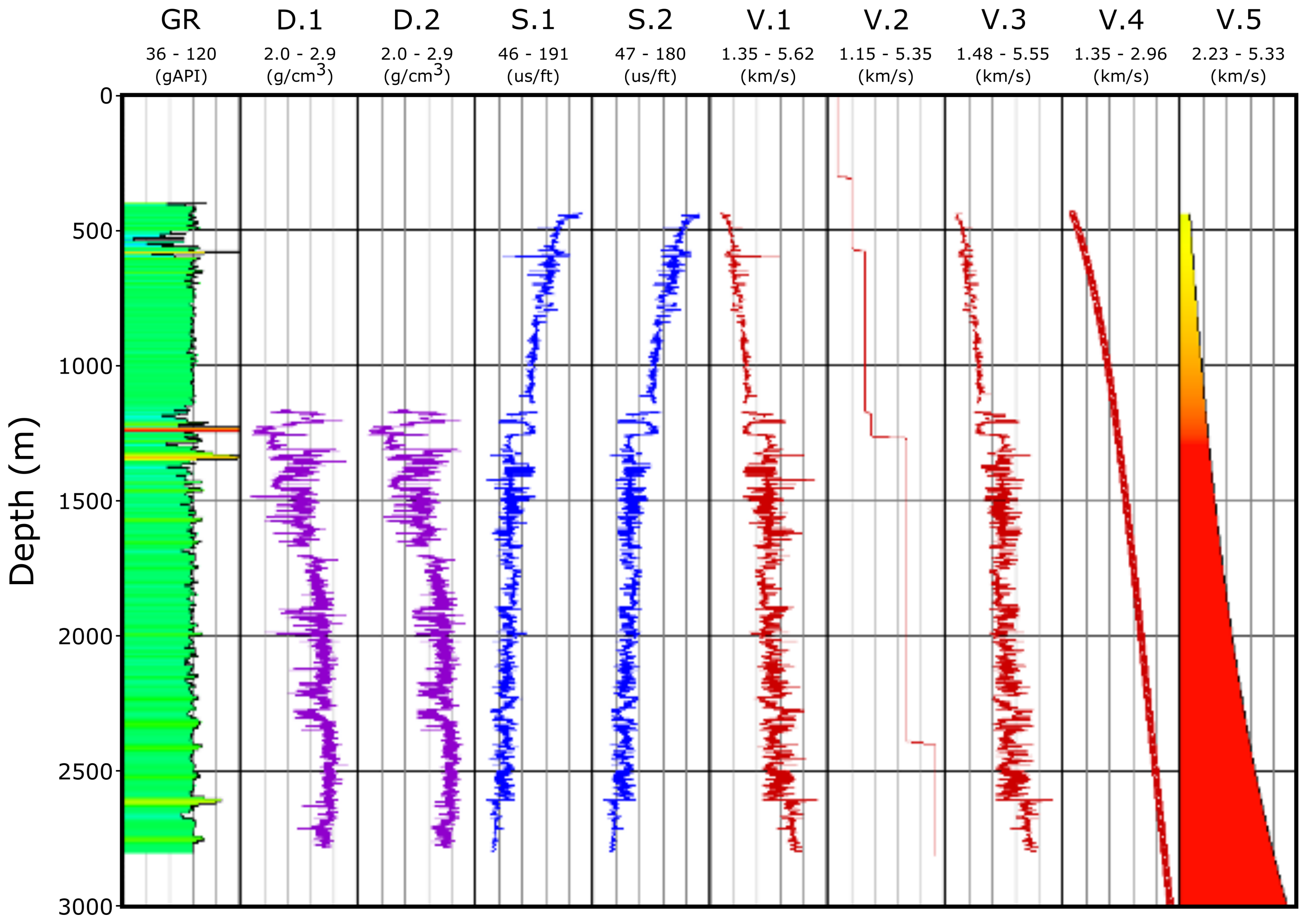

Figure 2. Well section view showing wireline and calculated logs for wellbore 7124/4-1S. The displayed data are for gamma ray (GR), density log (D.1), filtered density log (D.2), sonic log (S.1), filtered sonic log (S.2), calculated velocity from sonic log (V.1), modelled interval velocity using simplified geological model (V.2), calculated velocity from filtered sonic log (V.3), calculated average velocity using estimated time-depth relationship from first seismic well tie (V.4), calculated pseudo interval velocity using estimated time-depth relationship from second seismic well tie (V.5).

A

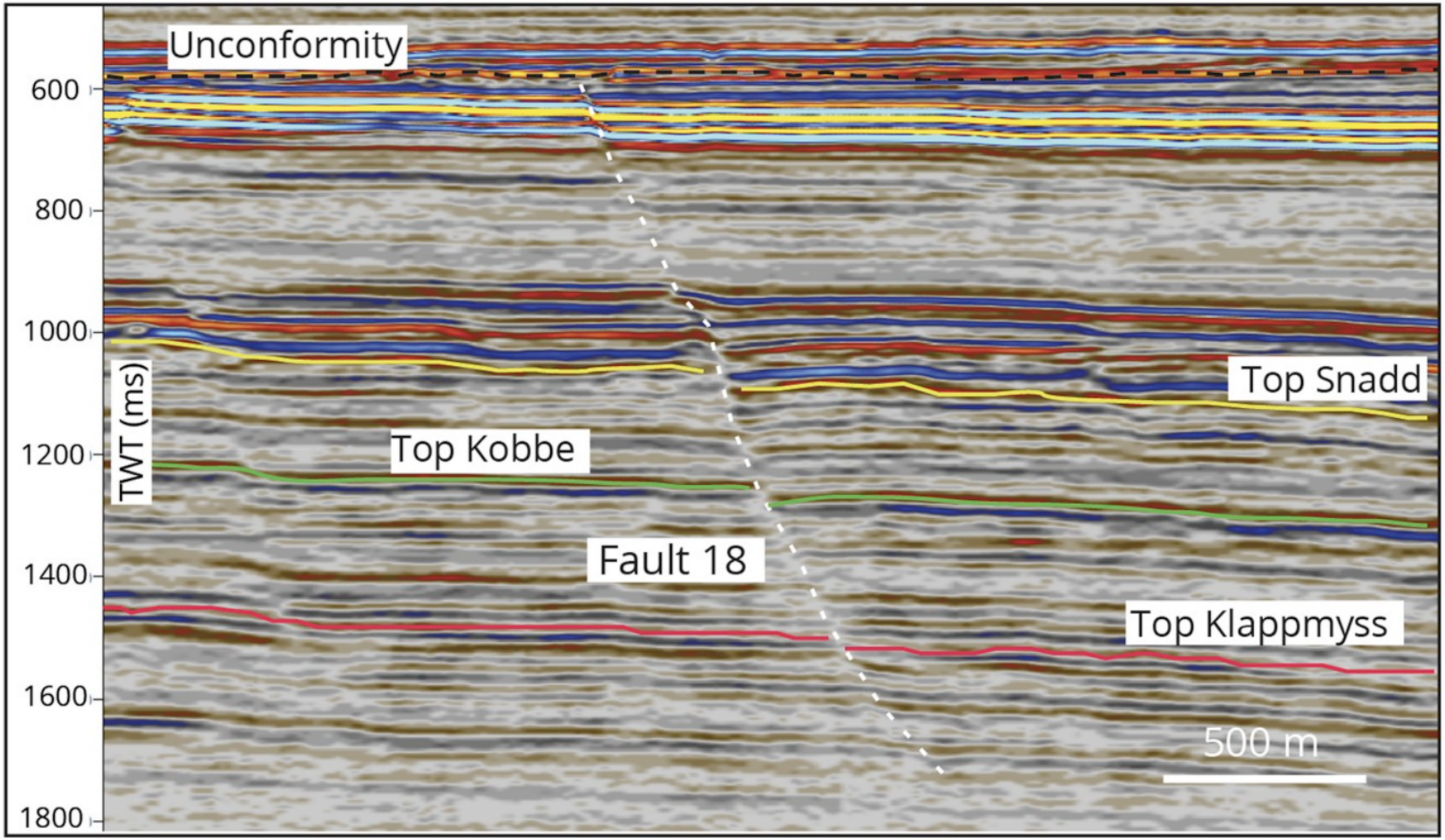

Unconformity
600
800
1000
1200
1400
1600
1800
TWT (ms)
Top Snadd
Top Kobbe
Fault 18
Top Klappmyss
500 m

B

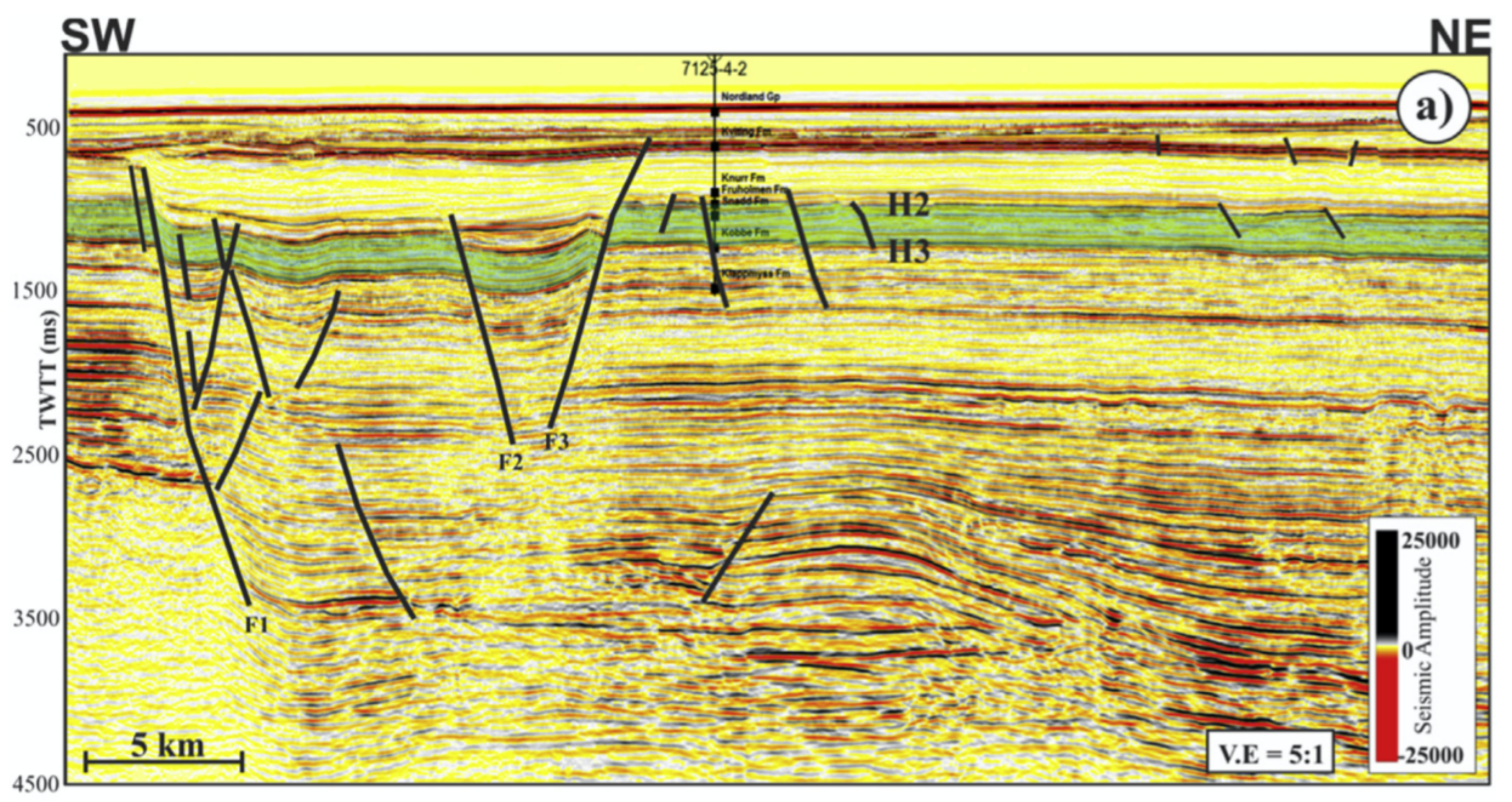
SW
NE
7125-4-2
Nordland Gp
Knurr Fm
Fruholmen Fm
Snadd Fm
Kobbe Fm
a)
H2
H3
F1
F2
F3
500
1500
2500
3500
4500
TWTT (ms)
5 km
V.E = 5:1
25000
0
-25000
Seismic Amplitude

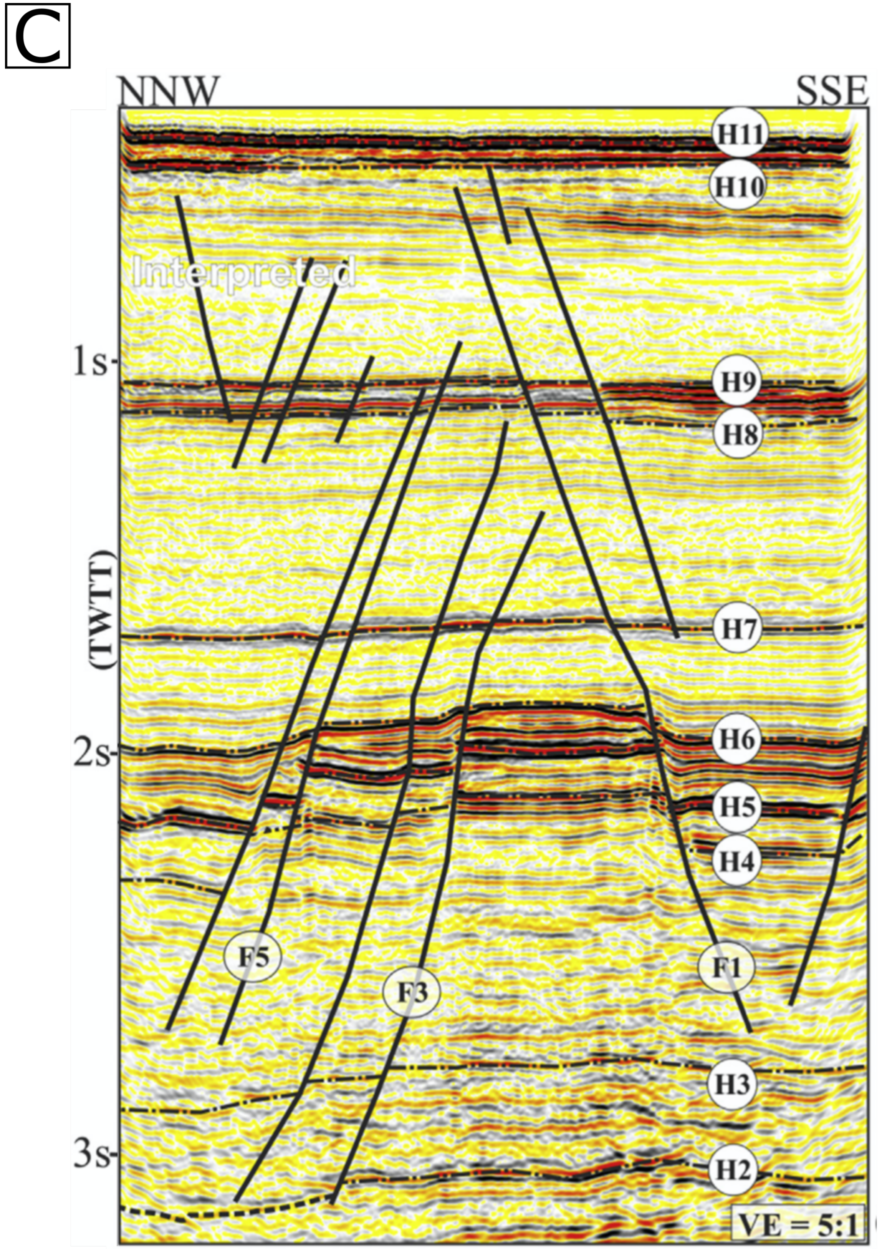
C
NNW
SSE
Interpreted
H11
H10
H9
H8
H7
H6
H5
H4
H3
H2
F5
F3
F1
1s
2s
3s
(TWTT)
VE = 5:1

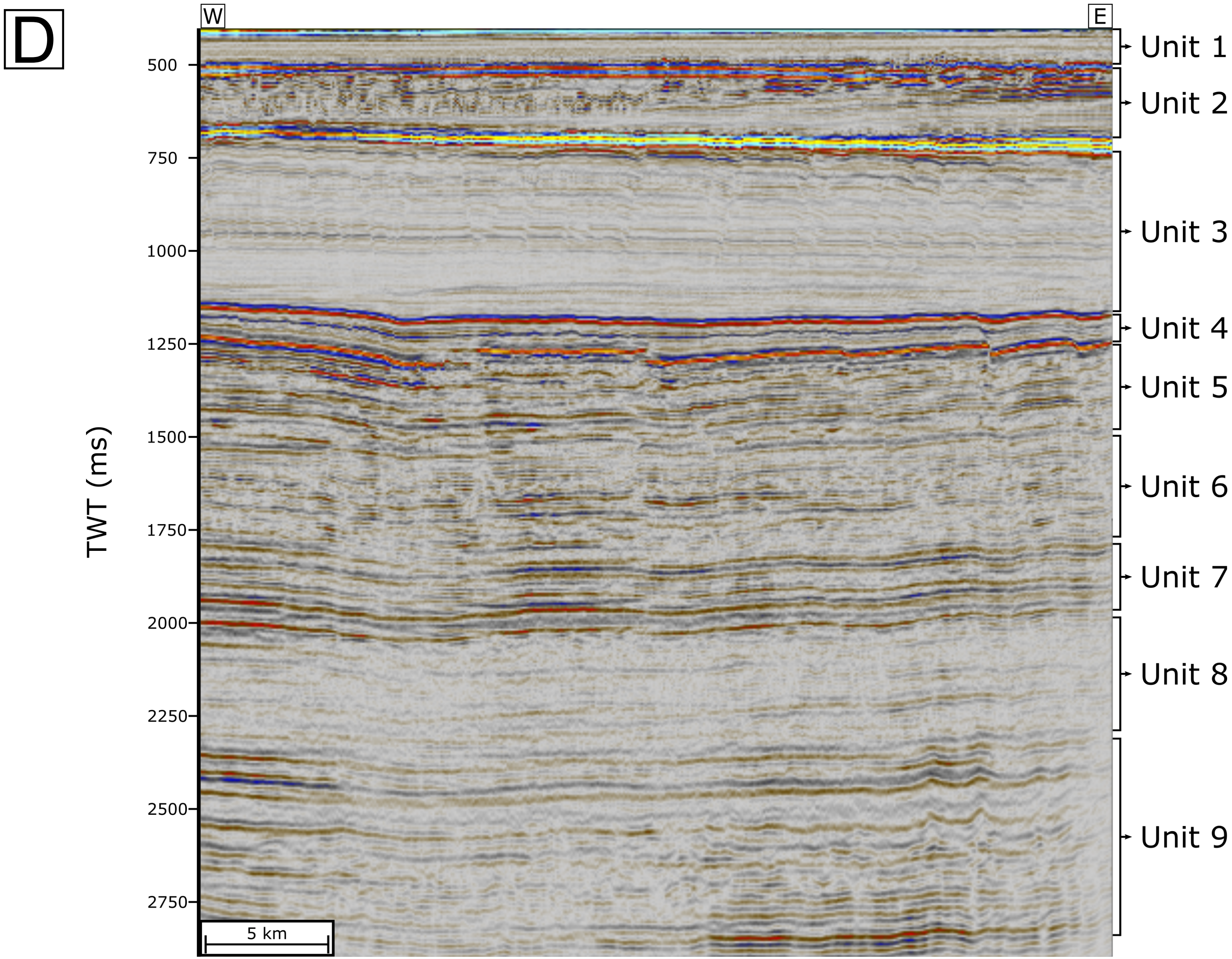

Figure 3. Representative seismic sections used for qualitative seismic stratigraphic correlation with offset well (A: Torabi et al., 2019; B: Harishidayat et al., 2015; C: Mohammedyasin et al., 2016; D: our study area). Detail description of seismic facies and age assignment for section D are shown on Table.1.

Expansion Index Analysis

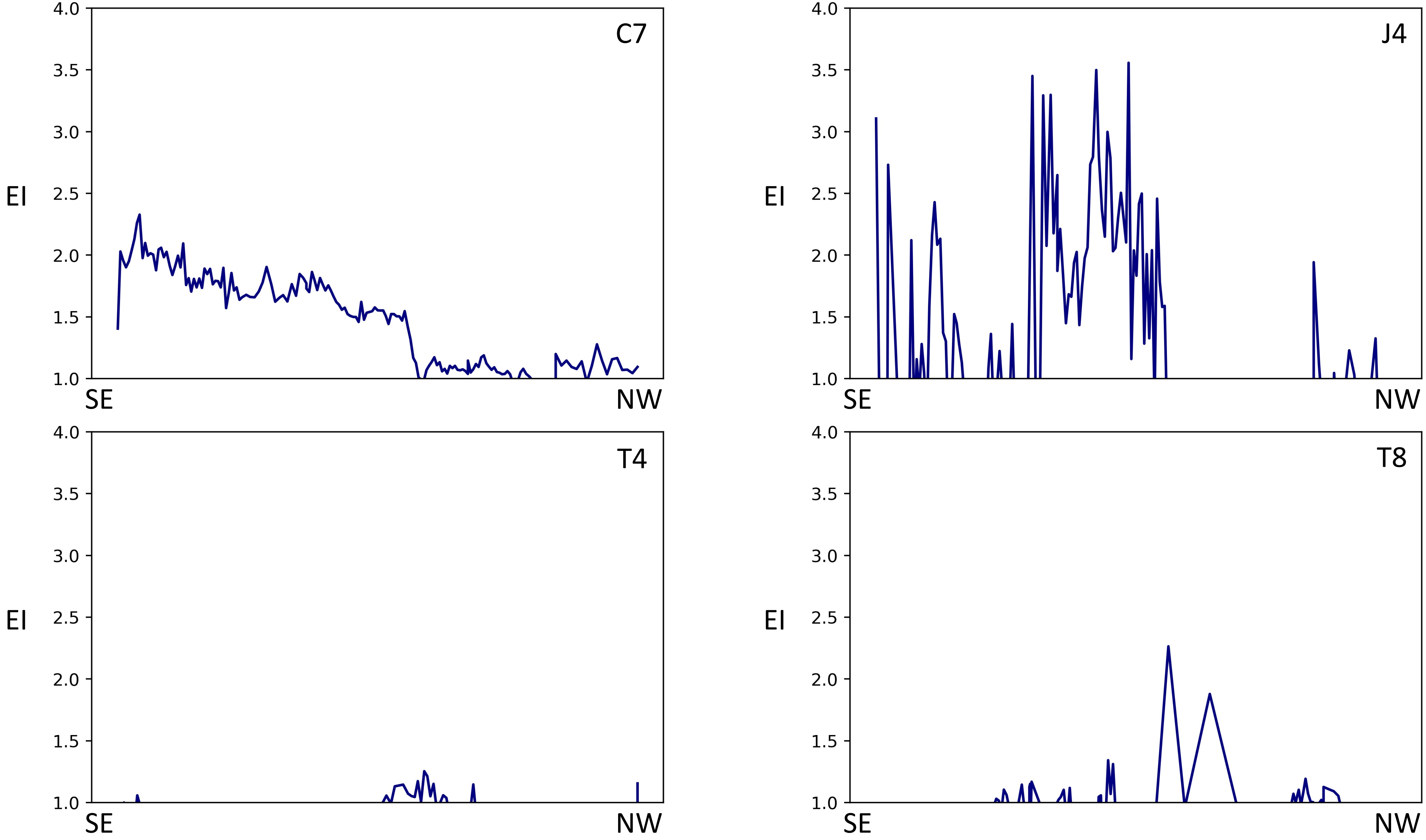

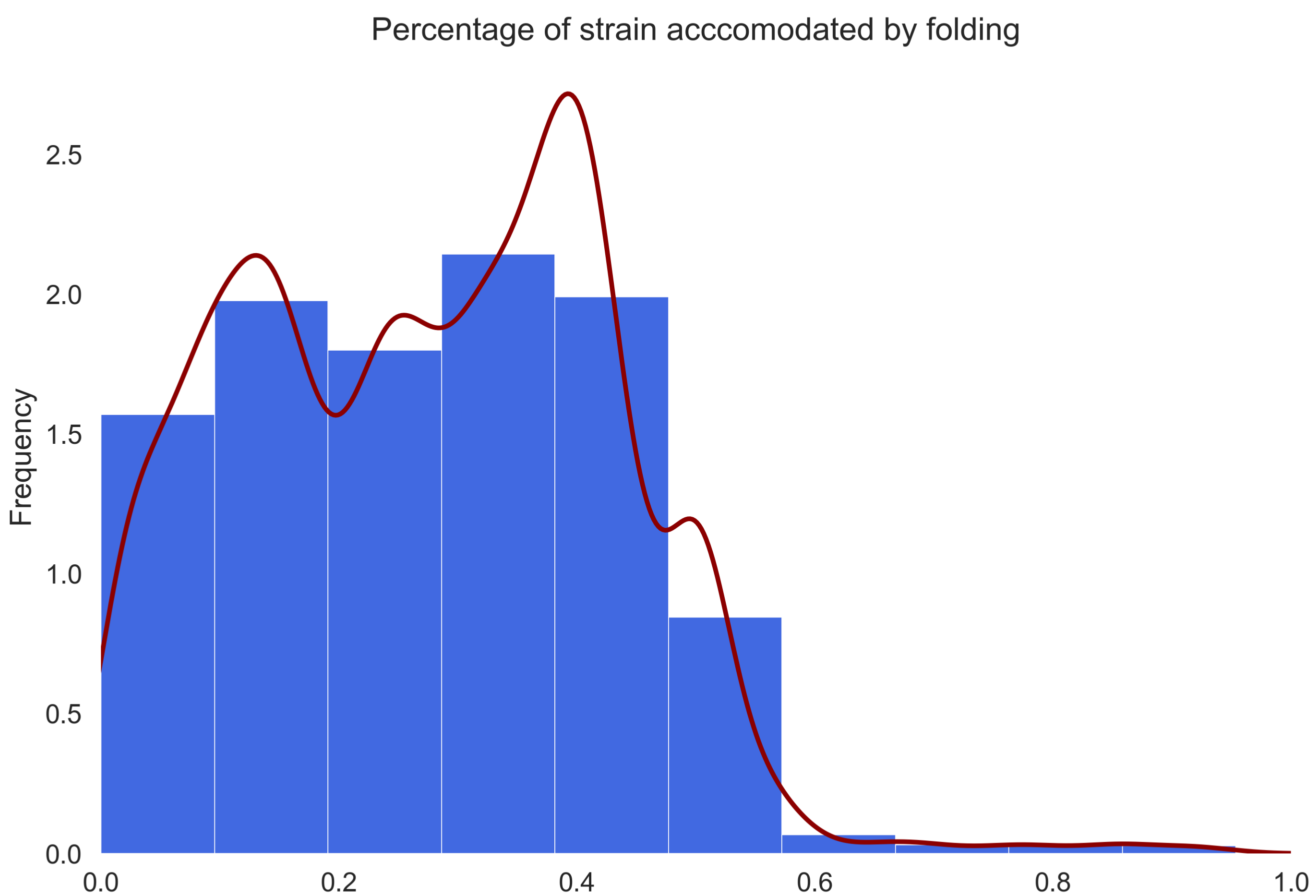
Percentage of strain acccomodated by folding
Frequency
2.5
2.0
1.5
1.0
0.5
0.0
0.0
0.2
0.4
0.6
0.8
1.0